*Annual Review of Astronomy and Astrophysics*

# The Interstellar Interlopers

David Jewitt[1] and Darryl Z. Seligman[2]

[1]Department of Earth, Planetary and Space Sciences, University of California, Los Angeles, California, USA; email: jewitt@ucla.edu

[2]Department of Astronomy and Carl Sagan Institute, Cornell University, Ithaca, New York, USA; email: dzs9@cornell.edu



Annu. Rev. Astron. Astrophys. 2023. 61:197–236

First published as a Review in Advance on June 7, 2023

The *Annual Review of Astronomy and Astrophysics* is online at astro.annualreviews.org

https://doi.org/10.1146/annurev-astro-071221-054221



## Keywords

comets, interstellar interlopers, protoplanetary disk

## Abstract

Interstellar interlopers are bodies formed outside of the Solar System but observed passing through it. The first two identified interlopers, 1I/'Oumuamua and 2I/Borisov, exhibited unexpectedly different physical properties. 1I/'Oumuamua appeared unresolved and asteroid-like, whereas 2I/Borisov was a more comet-like source of both gas and dust. Both objects moved under the action of nongravitational acceleration. These interlopers and their divergent properties provide our only window so far onto an enormous and previously unknown galactic population. The number density of such objects is $\sim$0.1 AU$^{-3}$ which, if uniform across the galactic disk, would imply $10^{25}$ to $10^{26}$ similar objects in the Milky Way. The interlopers likely formed in, and were ejected from, the protoplanetary disks of young stars. However, we currently possess too little data to firmly reject other explanations.

- 1I/'Oumuamua and 2I/Borisov are both gravitationally unbound, subkilometer bodies showing nongravitational acceleration.
- The acceleration of 1I/'Oumuamua in the absence of measurable mass loss requires either a strained explanation in terms of recoil from sublimating supervolatiles or the action of radiation pressure on a nucleus with an ultralow mass column density, $\sim$1 kg m$^{-2}$.
- 2I/Borisov is a strong source of CO and $H_2O$, which together account for its activity and nongravitational acceleration.
- The interlopers are most likely planetesimals from the protoplanetary disks of other stars, ejected by gravitational scattering from planets. 1I/'Oumuamua and 2I/Borisov have dynamical ages $\sim10^8$ and $\sim10^9$ years, respectively.

- Forthcoming observatories should detect interstellar interlopers every year, which will provide a rapid boost to our knowledge of the population.



## Contents



## 1. BACKGROUND

Tiny solid particles of dust carry about 1% of the mass of the interstellar medium (ISM). Mostly formed in the expanding, unstable atmospheres of evolved stars, these particles have characteristic sizes of ~0.2 to 0.3 μm or less. Until recently, the existence, abundance, and nature of possible macroscopic (meter-sized and larger) interstellar bodies have been a matter for speculation only. With the discovery of 1I/'Oumuamua and 2I/Borisov, two subkilometer bodies passing through the Solar System but formed elsewhere, the new population of macroscopic interstellar interlopers has finally been revealed.

The large sizes of the interlopers imply formation in dense environments, presumably the protoplanetary disks where interstellar dust hierarchically accumulates to form planets. Gravitational scattering by growing planets can excite the velocity dispersion of planetesimals, launching some beyond the control of the parent star. Judging from our own Solar System, most of the mass of the protoplanetary disk, and most of the material ejected to the ISM by planetary scattering,

originated in the cold regions beyond the $H_2O$ snow line. This freeze-out line is currently close to the orbit of Jupiter in our Solar System. The ice-rich material draws an immediate parallel between the expected properties of the interstellar bodies and those of the comets native to the Solar System, which we briefly discuss here.

Solar system comets are divided into two distinct dynamical types corresponding to two distinct long-term storage reservoirs. The short-period comets (SPCs), with modest eccentricities ($e < 1$) and inclinations, are derived from the trans-Neptunian Kuiper belt (specifically, from the scattered disk component of the Kuiper belt) by long-term chaotic instabilities (Volk & Malhotra 2008). The mass of the present-day Kuiper belt is $\sim$0.1 $M_\oplus$ (reduced from an estimated starting mass of $\sim$20 $M_\oplus$ or 30 $M_\oplus$). The belt contains $\sim 10^5$ bodies that are larger than 100 km and perhaps $\sim 10^{10}$ of kilometer-size. Some Kuiper belt objects (KBOs; the so-called "cold classical" objects) likely formed in situ (Parker & Kavelaars 2010, Nesvorný 2018), whereas other components of the belt are suspected to have formed at smaller distances and were subsequently scattered out gravitationally.

In contrast, the long-period comets (LPCs) have an isotropic distribution of inclinations, large semimajor axes, and eccentricities, $e \sim 1$ (**Figure 1**). Their source is the Oort cloud, a 50,000-AU-scale gravitationally bound swarm estimated to contain $N_{OC} \sim 10^{11}$ (Francis 2005) to $10^{12}$ (Brasser & Morbidelli 2013, Dones et al. 2015) 1-km-sized comets, as first recognized by Oort (1950). Although values for the total mass of the Oort cloud of $\sim$1 $M_\oplus$ are widely quoted, masses up to $\sim$20 $M_\oplus$ (Francis 2005) are allowed by the data. This is because the sizes and size distribution of LPC nuclei are poorly known and because the inner Oort cloud (semimajor axes $\lesssim$few $\times 10^3$ AU) might contain substantial mass and yet go undetected, because it is relatively immune to external perturbations (but see Kaib & Quinn 2009). Even during the earliest stages of planetary formation, typical densities at Oort cloud distances were too low for comets to have formed in situ there. Instead, the LPCs likely formed in the region now occupied by the giant planets, whose growth resulted in the gravitational scattering of many comets into highly eccentric and unbound ($e > 1$) orbits. A fraction of those ejected comets, $0.01 \lesssim f \lesssim 0.1$ (Hahn & Malhotra 1999, Brasser et al. 2010), became captured [by external perturbations from nearby stars, perhaps in the Sun's birth cluster (Dones et al. 2015), and by the galactic tide] into circularized orbits with

**Short-period comet (SPC):** nominally a comet with orbital period <200 years; most originate from the Kuiper belt

**Long-period comet (LPC):** nominally a comet with orbital period >200 years; most originate from the Oort cloud

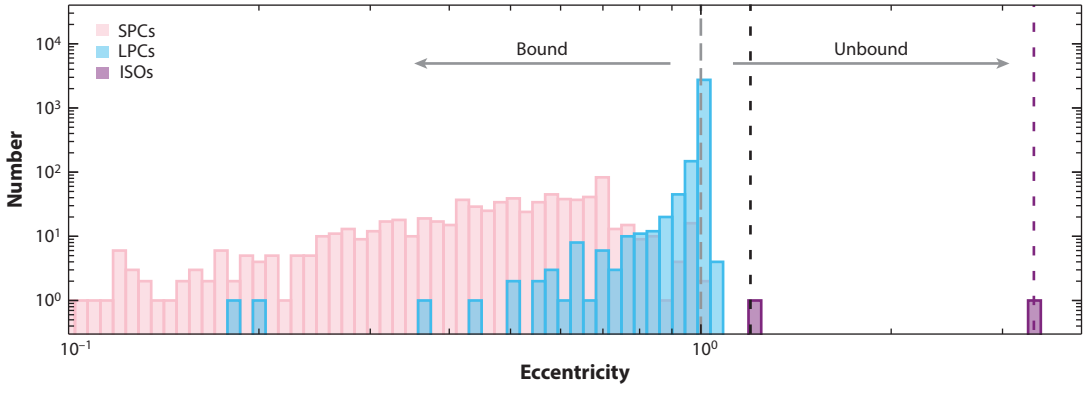


**Figure 1**

The distribution of osculating orbital eccentricities of LPCs (*blue*), SPCs (*pink*), and ISOs (*purple*). The dashed gray line indicates $e = 1$, separating bound from unbound orbits. The LPCs cluster at $e \simeq 1$. The eccentricities of 1I and 2I are indicated with black and purple dotted lines, respectively. These data are from the NASA JPL Horizons website, **https://ssd.jpl.nasa.gov/horizons/**. Abbreviations: ISO, interstellar object; LPC, long-period comet; SPC, short-period comet.

raised perihelia. Once removed from the gravitational control of the planets, the inclinations of these captured orbits were randomized over the course of several gigayears, transforming the initial disk-like distribution into the spherical, modern-day Oort cloud (Higuchi & Kokubo 2015). Continuing external perturbations on the Oort cloud supply LPCs back to the planetary region while dispersing others to interstellar space.

The remaining $(1 - f) \simeq 90$–$99\%$ of the ejected objects were lost by the Sun to the ISM. For example, taking $f = 0.01$, as many as $N_{OC}/f \sim 10^{13}$ to $10^{14}$ comets were ejected from the Solar System alone. Given $N_\star \sim 10^{11}$ stars in the galaxy, and assuming that all stars have Sun-like comet populations, a first-order guess as to the number of ejected comets in the galaxy is $N_{ii} = N_\star N_{OC}/f \sim 10^{24}$ to $10^{25}$. The combined mass of this population is a large but very uncertain $\sim 10^6$ $M_\odot$ to $\sim 10^7$ $M_\odot$ (assuming a nominal 1-km radius, as is typical of the measured comets). Depending on the nucleus size distribution, the total ejected mass could be much larger, as could the numbers of ejected subkilometer comets.

These simplified estimates are necessarily extrapolations based on limited knowledge. As discussed previously, the fraction of scattered comets that remained bound to the Solar System is uncertain by an order of magnitude. Furthermore, the analogous fraction for other stars depends sensitively on the architecture of their planetary systems and on the star cluster environment when they formed. The ejection and capture efficiencies must therefore differ from star to star, perhaps by large factors. Nevertheless, the serendipitous discoveries of 1I/'Oumuamua and 2I/Borisov prove the existence of a vast galactic population of macroscopic interlopers beyond reasonable doubt. There is explosive interest in both the physical nature and the possible origins of the galactic reservoir of interstellar interlopers.

## 2. DYNAMICAL PROPERTIES

The basic dynamical properties of the first two interstellar interlopers are summarized in **Table 1**, whereas their appearances at optical wavelengths are shown in **Figure 2**.

### 2.1. Discovery and Orbits

Small star system bodies are commonly discovered by wide-field sky surveys directed to other scientific objectives, as is true for both 1I/'Oumuamua and 2I/Borisov. The orbits of such objects are then determined from time-resolved astrometry, becoming increasingly accurate as the observational arc lengthens.

**2.1.1. 1I/'Oumuamua.** The first confirmed interstellar object (formerly C/2017 U1) was discovered by Robert Weryk on October 19, 2017, from the summit of Haleakalā on Maui, Hawaii (announced as 2017 U1 in Williams et al. 2017). Observations soon revealed that the orbit was hyperbolic. Specifically, the object had an osculating eccentricity $e = 1.201$, retrograde inclination

**Table 1 Dynamical properties of the interstellar interlopers**[a,b]

| Object | $T_P$ | $a$ (AU) | $e$ | $i$ (deg) | $q$ (AU) | $10^8 A_1$ (AU d$^{-2}$) | $10^8 A_2$ (AU d$^{-2}$) | $10^8 A_3$ (AU d$^{-2}$) | $\alpha_{ng}(1)$ (m s$^{-2}$) |
|---|---|---|---|---|---|---|---|---|---|
| 1I | September 9, 2017 | −1.272 | 1.198 | 122.8 | 0.252 | 27.9 ± 3.6 | 1.4 ± 2.4 | 1.6 ± 2.2 | $5.6 \times 10^{-6}$ |
| 2I | December 8, 2019 | −0.850 | 3.363 | 44.0 | 2.009 | 7.1 ± 0.8 | −1.4 ± 0.3 | 0.1 ± 0.1 | $1.5 \times 10^{-6}$ |

[a] $T_P$ is the date of perihelion; $a$, $e$, $i$, and $q$ are barycentric pre-entry orbital elements computed for January 1, 1900. $a < 0$ denotes hyperbolic orbit. Data from JPL Horizons.

[b] $A_1$, $A_2$, $A_3$, and $\alpha_{ng}(1)$ are nongravitational parameters from JPL Horizons, described in Section 2.2.

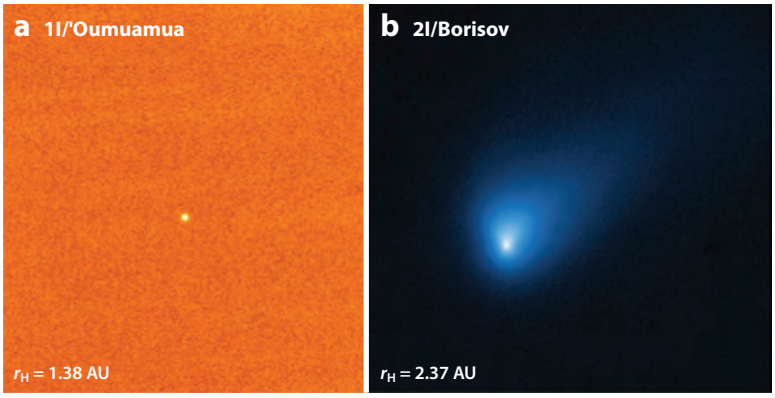


**Figure 2**

(*a*) 1I/'Oumuamua showing point-like appearance on UT October 26, 2017, at the 2.5-m Nordic Optical Telescope. (*b*) 2I/Borisov showing cometary activity on UT October 12, 2019, from the 2.4-m *Hubble Space Telescope*. The height of each panel corresponds to about 50,000 km. Abbreviation: UT, Universal Time.

$i = 122.8$ deg, and a perihelion distance $q = 0.256$ AU. (Removal of planetary perturbations gives only slightly different pre-entry barycentric orbital elements, as listed in **Table 1**). **Figure 3** shows the trajectory of 'Oumuamua and its position on October 17, 2017. 'Oumuamua was discovered close to Earth, passing within only about 0.16 AU three days prior to discovery. This serendipitous detection near the peak of ground-based visibility implies the existence of an unnoticed population of similar objects with less favorable observing geometries. 1I/'Oumuamua was point-like in all observations (**Figure 2**).

**2.1.2. 2I/Borisov.** The second known interstellar interloper, 2I/Borisov (also known as C/2019 Q4), was discovered on UT (Universal Time) August 30, 2019, when only 38 deg from the Sun. This remarkable observation was made by Gennadiy Borisov, who used a 0.65-m self-built telescope to target an area of the sky barely examined by other survey telescopes. Its orbit is robustly

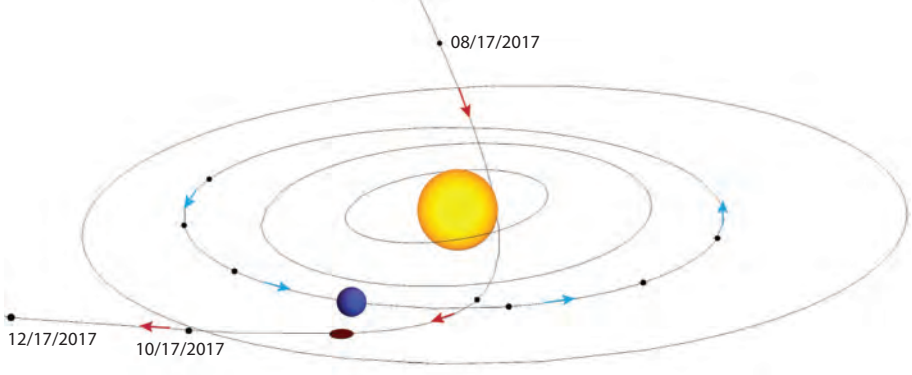


**Figure 3**

The trajectory of 1I/'Oumuamua near perihelion, from August to December 2017. The positions of Earth and 'Oumuamua at discovery on October 17 are indicated. Black points indicate the positions of Earth and 'Oumuamua at time intervals of one month. Arrows indicate the directions of motion of both objects around their orbits.

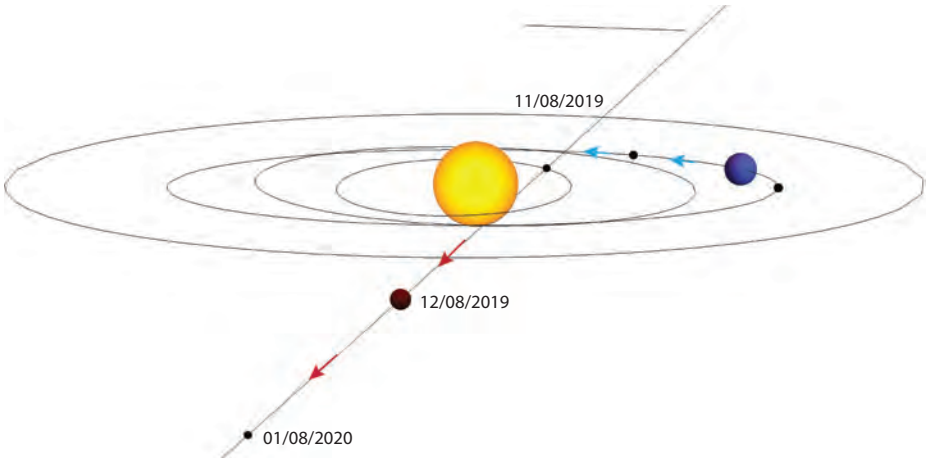


**Figure 4**

The trajectory of 2I/Borisov. The positions of Earth and 2I/Borisov at discovery are marked, with month-separated points as in **Figure 3**.

hyperbolic with eccentricity $e = 3.358$, and consequently the interstellar origin of 2I is not in doubt. 'Oumuamua was discovered outbound from perihelion only by virtue of its close approach to Earth, and it was only observable for a short time span. In sharp contrast—and fortunately—2I/Borisov was discovered about three months before perihelion (UT December 8, 2019, at $q = 2.00$ AU) because of its bright coma of ejected dust (**Figure 2**). The early discovery and intrinsic brightness of 2I/Borisov enabled physical and astrometric observations to be obtained for about 1 year, whereas 'Oumuamua faded beyond detection in only 2.5 months. The trajectory of 2I/Borisov is shown schematically in **Figure 4**.

## 2.2. Nongravitational Acceleration

The motions of some solar system bodies cannot be fitted using purely gravitational solutions. Additional, so-called nongravitational forces include both very weak radiation forces and much stronger recoil forces due to the anisotropic ejection of mass.

**2.2.1. 1I/'Oumuamua.** Observations over a 2.5-month arc allowed an accurate determination of the orbit of 'Oumuamua and unexpectedly revealed the existence of nongravitational acceleration. In active comets, nongravitational acceleration is caused by recoil from the asymmetric ejection of mass. Its detection in 1I/'Oumuamua was especially puzzling because observations provided no evidence for mass loss at any level. By convention, such accelerations are described by three orthogonal components, $A_1, A_2$, and $A_3$, each expressed as AU day$^{-2}$. Here, $A_1$ is the acceleration away from the Sun, $A_3$ is perpendicular to the orbit plane, and $A_2$ completes the right-handed triple. The total acceleration at $r_H = 1$ AU is computed from $\alpha_{ng}(1) = g(r_H)(A_1^2 + A_2^2 + A_3^3)^{1/2}$ and is expressed in m s$^{-2}$ (see **Table 1**). The quantity $g(r_H)$ is a function that represents the radial dependence of the mass loss, normalized such that $g(1\text{ AU}) = 1$ (Marsden et al. 1973). **Table 1** lists the accelerations provided by JPL Horizons[1] and shows that $A_1$ is the dominant component. This is consistent with a force acting radially away from the Sun, as expected of outgassing recoil

[1] **https://ssd.jpl.nasa.gov/horizons/app.html**.

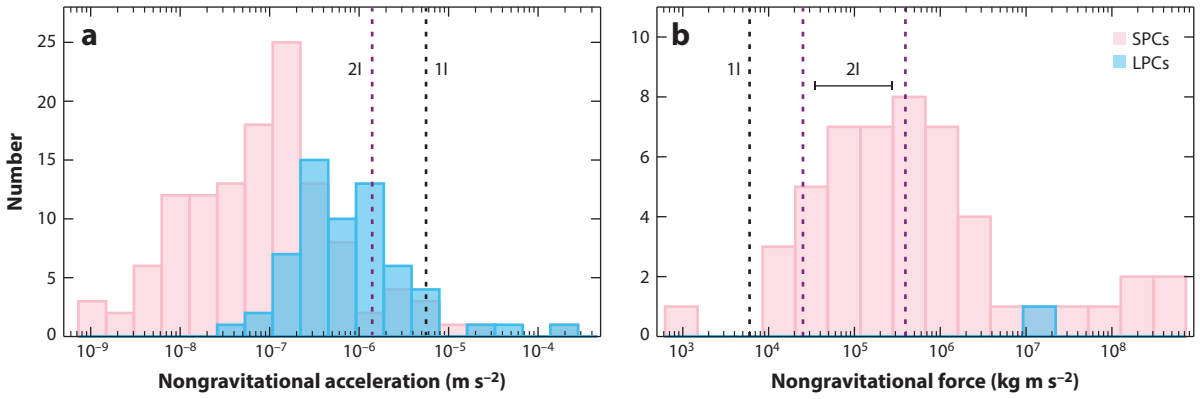


**Figure 5**

(*a*) Dashed lines show the measured nongravitational accelerations of 1I/'Oumuamua and 2I/Borisov compared to values for SPCs (*pink*) and LPCs (*blue*). (*b*) Nongravitational force computed assuming spherical nuclei and a bulk density $\rho = 500$ kg m$^{-3}$. For the interlopers, we use object radii as listed in **Table 2**; 2I is represented by a range to reflect the uncertainty of the radius. Nongravitational accelerations and nucleus diameters are taken from the JPL Small Body Database. The sizes (hence, masses) of LPCs are largely unknown. Abbreviations: LPC, long-period comet; SPC, short-period comet.

(see Section 4.1) and radiation pressure (Section 4.2). The magnitude of the acceleration, $\alpha_{ng}(1)$, corresponds to about $10^{-3}$ times the local solar gravitational acceleration at 1 AU.

**2.2.2. 2I/Borisov.** A 10-month astrometric series also revealed nongravitational acceleration in 2I/Borisov, with $A_1$ again being the dominant component and with a smaller magnitude (**Table 1**). Unlike the case of 1I/'Oumuamua, the nongravitational acceleration of 2I/Borisov was matched by obvious, ongoing mass loss, and the cause is not mysterious.

**Figure 5** compares the nongravitational accelerations (panel *a*) and forces (panel *b*) acting on the comets and interlopers. A comparison shows that though the acceleration of 'Oumuamua is larger than in most comets, this is simply because it is very small and few subkilometer comets are known (all else being equal, we expect acceleration $\alpha_{ng}(1) \propto r_n^{-1}$). When plotted as force, 1I is on the weaker side of the comet distribution, which is consistent with a low rate of mass loss. The larger nucleus of 2I/Borisov shows a high but less extreme value of $\alpha_{ng}(1)$ but is unremarkable on the histogram of forces in the figure. However, these are not direct comparisons because most Solar System comets are larger than both 'Oumuamua and Borisov. In both interlopers, $\alpha_{ng}$ varies with heliocentric distance approximately as $r_H^{-2}$, although the heliocentric dependence is not well measured because of the limited range of distances over which astrometric observations were secured.

## 3. PHYSICAL PROPERTIES

Key physical properties of 1I/'Oumuamua and 2I/Borisov are summarized in **Table 2** and more fully discussed in the following text.

### 3.1. Nucleus Sizes

The apparent magnitude of an object viewed in reflected sunlight, $V$, is related to the albedo, $p$, and effective radius, $r_n$ by (Russell 1916),

$$p\,\Phi(\alpha)\,r_n^2 = \left(2.25 \times 10^{22}\right) r_H^2\,\Delta^2\,10^{0.4(V_\odot - V)}, \qquad 1.$$

**Table 2 Physical properties of the interstellar interlopers**[a]

| Object | Radius, $r_n$[b] (m) | Radius, $r_n$[c] (m) | Period, P[d] (hour) | Shape | $b/a$[e] | $S'$[f] (%/1000 Å) | $\dot{M}$[g] (kg s$^{-1}$) |
|---|---|---|---|---|---|---|---|
| 1I | 55–114 | 80 | ~8 | Oblate | ~6:1 | 15 ± 5 | <$10^{-3}$ |
| 2I | 200–500 | 400 | NA | NA | NA | 12 ± 1 | ~20 to 40 |

Abbreviation: NA, not available.
[a]Approximate physical properties as described in the text, with sources as in Section 3.
[b]Range of reported radii, expressed as the radius of an equal-area circle, albedo $p = 0.1$ assumed.
[c]Nominal radius adopted in this work.
[d]Nucleus rotation period.
[e]Ratio of the nucleus semiaxes.
[f]Reflectivity gradient (Sun = 0).
[g]Measured dust mass loss rate.

where $r_H$ and $\Delta$ are the heliocentric and geocentric distances in astronomical units, $\alpha$ is the phase (Sun-object-observer) angle, and $V_\odot$ is the apparent magnitude of the Sun. The phase function, $\Phi(\alpha)$, represents the dimming of the object observed at phase angle $\alpha$ relative to $\alpha = 0$. Given only optical observations, the number of unknowns [$p$, $r_n$, and $\Phi(\alpha)$] in Equation 1 exceeds the number of constraints. Therefore, there is ambiguity in estimates of $r_n$ depending on the assumed values of $p$ and $\Phi(\alpha)$. Additional complications arise because published observations use different filters and assume different phase functions and geometric albedos. Albedos of fresh icy surfaces tend to be large, $p \sim 0.8$–$0.9$, whereas the carbonaceous surfaces of primitive asteroids tend to be small, $p \sim 0.04$. To proceed, we scale relevant properties assuming that $p = 0.1$.

With this albedo, the effective nuclear radius of 'Oumuamua lies in the range of 55 m (Jewitt et al. 2017) to 70 ± 3 m (Meech et al. 2017), to 80 m (Drahus et al. 2018), to 114 m (Knight et al. 2017). With no objective way to decide among these estimates, we take a middle value, $r_n$ = 80 m, as our best estimate of the effective radius, included in **Table 2**, and note that this value is uncertain by a factor on the order of two.

The bright coma prevented direct detection of the nucleus of 2I/Borisov. However, Jewitt et al. (2020a) constrained the nuclear radius to lie within the range $0.2 \leq r_n \leq 0.5$ km. The upper limit is set by the nondetection of the nucleus in high-resolution surface brightness data. The lower limit is derived from the nongravitational acceleration assuming a comet-like bulk density $\rho_n$ = 500 kg m$^{-3}$. We adopt $r_n$ = 400 m as the nominal value.

## 3.2. Colors

Broadband colors are not compositionally diagnostic, but they do provide another metric with which to compare the interlopers with other Solar System bodies. The conventional reference point is provided by the color of the Sun, which has optical color index B-R = 0.99 ± 0.02. For objects in which the albedo varies linearly with wavelength, as is commonly the case in distant Solar System bodies, it is useful to use the reflectivity gradient, defined as the fractional change in the brightness per unit wavelength, $S'$ [% (1000 Å)$^{-1}$], relative to that of the Sun. The Sun, by definition, has $S' = 0\%$ (1000 Å)$^{-1}$. Objects with B-R > 1.6, corresponding to $S' \sim 25\%$ (1000 Å)$^{-1}$, are described as containing ultrared matter (Jewitt 2002).

**Ultrared matter:** found in the cold-classical Kuiper belt objects and in a fraction of the Centaurs, ultrared matter has optical colors B-R > 1.6

**3.2.1. 1I/'Oumuamua.** Published optical measurements of the color of 'Oumuamua consistently show a surface reddened with respect to the Sun, but with wide scatter. This scatter reflects the difficulty of obtaining measurements for such a highly variable, rapidly moving target. The reflectivity increases linearly with wavelength from at least 4500 Å to 10500 Å (Meech et al. 2017, Fitzsimmons et al. 2018). Values of the spectral slope range from $S' = 7 \pm 3\%$/1000 Å

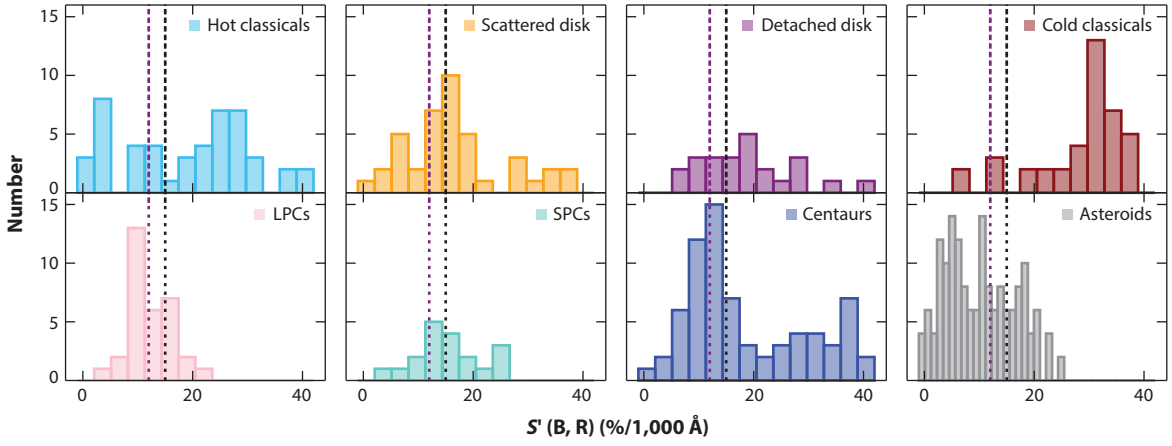


**Figure 6**

Color distributions of minor bodies in the Solar System compared with those of 'Oumuamua and 2I/Borisov (shown as *vertical dotted lines*). Slope $S' = 0\%$ (1000 Å)$^{-1}$ corresponds to the solar color B-R = 0.99, whereas $S' \sim 25\%$ (1000 Å)$^{-1}$ corresponds to B-R = 1.6. Colors are from Hainaut et al. (2012) and Warner et al. (2009).

(Jewitt et al. 2017) to 23 ± 3%/1000 Å (Meech et al. 2017); we adopt a middle value from independent measurements near $S' = 15 \pm 5\%$/1000 Å.

**3.2.2. 2I/Borisov.** Whereas the colors of 1I/'Oumuamua refer to the bare nucleus, those of 2I/Borisov measure the color of coma dust, with negligible contribution from the nucleus. As with the case of 'Oumuamua, reported measurements of the color of 2I show a reddened optical continuum with a scatter larger than the formal measurement errors (Jewitt & Luu 2019, Bolin et al. 2020, Guzik et al. 2020, Hui et al. 2020, Mazzotta Epifani et al. 2021). Some of these differences in measurements may be attributed to the usage of a variety of filters. Specifically, it is known that the U and B filters may be contaminated by resonance fluorescence bands from gas. The continuum color of 2I/Borisov might also have varied with time and distance from the Sun (Mazzotta Epifani et al. 2021). We adopt a nominal spectral slope of $S' \sim 12 \pm 1\%$ (1000 Å)$^{-1}$.

In **Figure 6**, we show the color distributions (expressed as $S'$) of different populations of minor bodies in the Solar System. These data are drawn from the online updated database[2] originally described by Hainaut et al. (2012). We also indicate the positions of 'Oumuamua and Borisov with respect to these distributions.

In the inner Solar System, the reddish colors of asteroids are due to an abundance of nanophase (1 to 100 nm) iron produced in surface materials by energetic particle bombardment ("space weathering"). Optical colors in the outer Solar System can be much redder. Ultrared colors probably reflect the presence of irradiated, macromolecular carbon compounds that are unstable or otherwise depleted in the warm, inner Solar System. The cold-classical KBOs are the least dynamically evolved objects in the belt and located at about 43 AU. They also exhibit a larger fraction of ultrared surface colors compared to most other small bodies in the Solar System, with the exception of the Centaurs (recently escaped KBOs). This difference is not understood and may be attributed to longer exposure to space weathering if the cold classicals formed in situ. The colors of 1I and 2I are similar to each other and to most inner Solar System populations (see **Figure 6**).

**Centaur:** centaurs are recently escaped Kuiper belt objects and a precursor stage to the Jupiter family comets

[2]MBOSS Database: **https://www.eso.org/~ohainaut/MBOSS/**.

The lack of distinctive evidence for ultrared matter, expected from long-term exposure to the interstellar environment, is consistent with the colors of LPCs.

## 3.3. Activity

Mass loss from small Solar System bodies is generally most prominent in optical images. This is because small dust particles present a very large scattering cross-section per unit mass and because dust can be ejected slowly (e.g., meters per second), allowing large column densities to build up. In comparison, the detection of gas is more challenging, both because molecular resonance fluorescence cross-sections are small and because the high gas outflow speeds (e.g., kilometers per second) dilute the column densities.

**3.3.1. 1I/'Oumuamua.** The morphology of 'Oumuamua was at all times point-like, even in the highest-resolution data from the *Hubble Space Telescope* and in the deepest data from large ground-based telescopes. The optical data provide no evidence for outgassing activity. The optical scattering cross sections of typical cometary comae are dominated by dust, with minor contributions from resonance fluorescence from gas molecules. Accordingly, measurements of the surface brightness profile of 'Oumuamua were used to place model-dependent limits on the mass loss in micron-sized dust particles; $\dot{M} \leq 2 \times 10^{-4}$ kg s$^{-1}$ (Jewitt et al. 2017), $\dot{M} \leq 2 \times 10^{-3}$ kg s$^{-1}$ (Meech et al. 2017) (see **Table 2**). Both upper limits are orders of magnitude smaller than the $10^2$ kg s$^{-1}$ to $10^3$ kg s$^{-1}$ mass-loss rates from typical near-Sun comets estimated in the same way. Limits on the production of water, the dominant cometary volatile, are $\dot{M} \leq 30$ kg s$^{-1}$, as determined from radio lines of the dissociation product, OH (see Section 3.5).

**3.3.2. 2I/Borisov.** In sharp contrast to 'Oumuamua, 2I displayed (and, indeed, was discovered because of) obvious cometary activity in the form of an extended optical dust coma (**Figure 2**; Jewitt & Luu 2019, Guzik et al. 2020). Dust dynamics models reproduce the slowly changing morphology of the comet (**Figure 7**) and show that the coma is dominated by submillimeter and larger particles (Kim et al. 2020, Yang et al. 2021). Total dust production rates estimated from imaging data alone range from $\dot{M} \sim 2$ kg s$^{-1}$ (Jewitt et al. 2020a) to $\dot{M} \sim 35$ kg s$^{-1}$ (Cremonese et al. 2020,

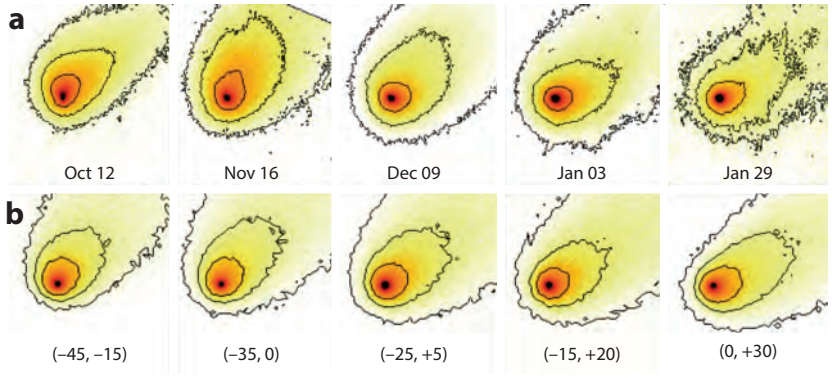


**Figure 7**

(*a*) Images and (*b*) dust dynamics models of 2I/Borisov as a function of date. The models indicate a coma consisting of large (effective size ~ 1 mm), slowly ejected ($V \sim 2$ m s$^{-1}$) particles in steady state. Small particles are more strongly swept by radiation pressure, creating a coma and tail unlike those observed. Figure adapted with permission from Kim et al. (2020).

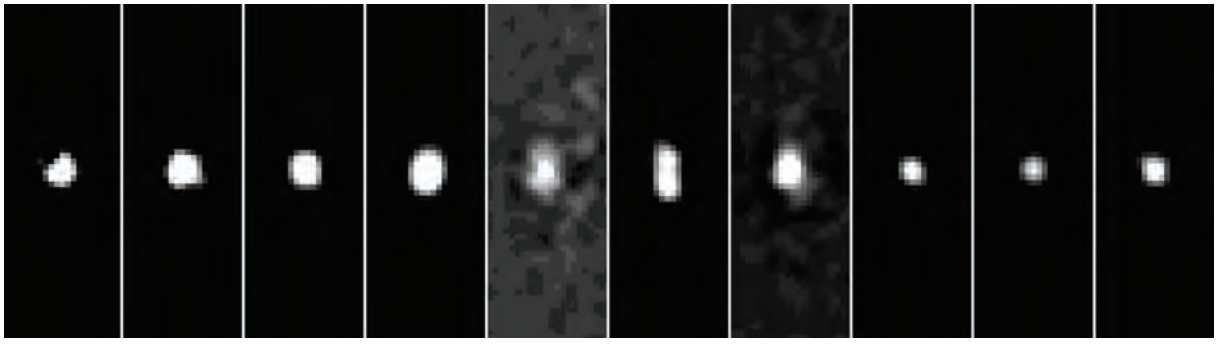


**Figure 8**

Spatially filtered (coma suppressed) *Hubble Space Telescope* images of 2I/Borisov showing the appearance of a split nucleus on UT March 30, 2020. Each panel shows a region 0.44-arcsec wide corresponding to about 800 km at the comet's distance. Note that the resolution of the telescope projects to ~150 km at the 2.65-AU geocentric distance of 2I/Borisov on March 30. Figure adapted from Jewitt et al. (2020b).

Kim et al. 2020). Less model-dependent spectroscopic production rates gave gas production rates up to $\dot{M} = 20$ to 40 kg s$^{-1}$.

Continued activity in 2I/Borisov included a photometric outburst (Drahus et al. 2020) and subsequent breakup, illustrated in **Figure 8** (Jewitt et al. 2020b). The postperihelion breakup might be related to a seasonal response, the likes of which are commonly observed in Solar System comets (Kim et al. 2020).

## 3.4. Light Curves

Most small solar system bodies exhibit periodic variations in brightness associated with their rotation. The light curves of those bodies can be used to measure both the rotational period and an estimate of the ratio of long to short axes, projected into the plane of the sky.

**3.4.1. 1I/'Oumuamua.** Photometric observations immediately showed that 'Oumuamua had an extremely large light curve peak-to-peak amplitude of $\Delta V \sim 2.5$ mag, corresponding to a factor of ~10 in brightness and a stable period close to 8 h (Bannister et al. 2017, Jewitt et al. 2017, Knight et al. 2017, Meech et al. 2017, Bolin et al. 2018, Drahus et al. 2018). The light curve is shown in **Figure 9**, adapted from the data in Belton et al. (2018, their figure 1). Although the period of 'Oumuamua is unremarkable compared with the distribution of rotational periods of the asteroids, the brightness variations are extreme (**Figure 10**), as is discussed below.

Light curves of atmosphereless Solar System bodies are caused by azimuthal shapes or surface albedo variations modulated by rotation. To first order, the shape of an irregular body projected into the sky-plane can be approximated as an ellipsoid with semiaxes $a \times b$. The "effective radius," equal to the radius of a circle having equal area, is simply $r_n = (ab)^{1/2}$ (**Table 2**). At opposition (Sun-target-Earth angle = 0 deg), the axis ratio $b/a$ is related to the apparent light curve amplitude, $\Delta V$ in magnitudes, by $b/a = 10^{0.4\Delta V}$. Substitution gives $b/a = 10{:}1$ for 'Oumuamua (Meech et al. 2017). However, most observations of 'Oumuamua were obtained at phase angles $\alpha \sim 20$ deg, where illumination and self-shadowing effects act to magnify the light curve amplitude relative to that at zero phase (Kaasalainen et al. 2001, Lacerda & Jewitt 2007, Lu & Jewitt 2019). Taking these effects into account, the projected axis ratio of 'Oumuamua corresponding to $\Delta V = 2.5$ mag is reduced to $b/a = 6{:}1$ or $7{:}1$ (Jewitt et al. 2017, Drahus et al. 2018, McNeill et al. 2018). This

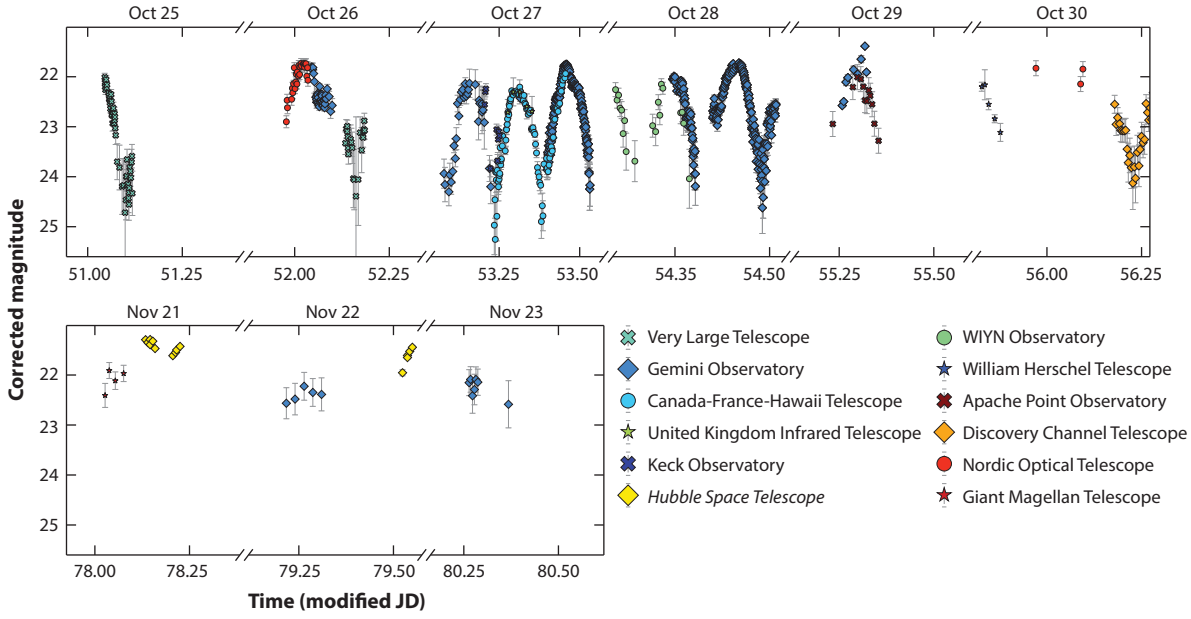


**Figure 9**

The photometric light curve of 'Oumuamua, similar to that computed by Belton et al. (2018). This figure uses the photometric data presented by Meech et al. (2017), Jewitt et al. (2017), Bannister et al. (2017), Bolin et al. (2018), Drahus et al. (2018), Knight et al. (2017), and Belton et al. (2018). The points are color coded based on the observational facility that obtained the data. Abbreviation: JD, Julian date.

is still an extreme shape compared to known Solar System bodies (cf. **Figure 10**). The shapes of the asteroids are controlled by repeated energetic and sometimes disruptive collisions. Even for these violent cases, the average projected axis ratios are $b/a \sim 1.4{:}1$ and values $b/a \geq 2$ are rare. With $b/a = 6{:}1$ and effective radius $r_n = 80$ m, the projected sky-plane shape of 'Oumuamua is an $a \times b = 32 \times 196$-m ellipse. It is worth noting that the NEO 2016 $AK_{193}$ exhibited brightness

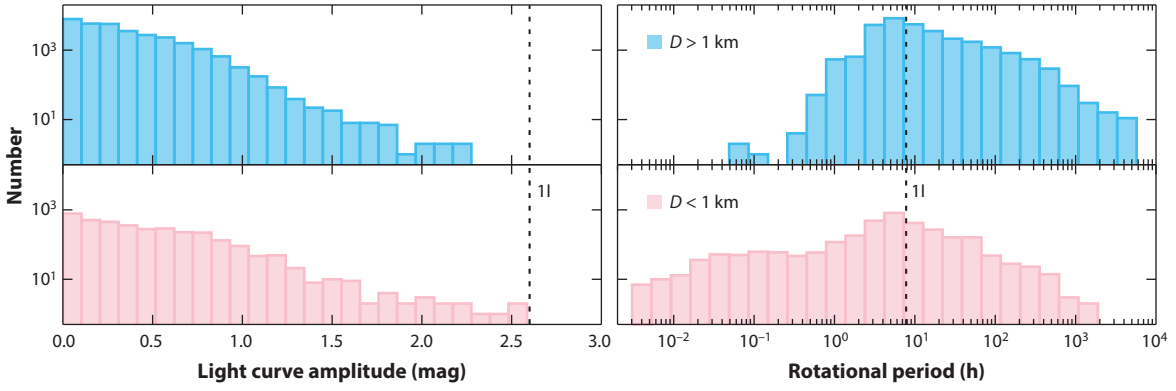


**Figure 10**

The distribution of asteroid light curve amplitudes (*left*) and rotational periods (*right*). The measured values for 'Oumuamua are shown as dotted black lines (these are unconstrained for Borisov). The top and bottom panels show the distribution for all objects greater than and less than 1 km in diameter, respectively. Data from Warner et al. (2009).

variations of ∼2.5–3 mag during its discovery apparition and subsequent follow-up observations (Heinze 2021).

Elongated Solar System bodies are typically prolate in shape and rotating around a minor axis. A large light curve amplitude can also be produced by an oblate body rotating around a long axis. Detailed numerical and analytic calculations performed by Mashchenko (2019) demonstrated that the most likely shape of 'Oumuamua was a 6:6:1 oblate ellipsoid, as opposed to the 6:1:1 prolate geometry popularized in several solicited artist impressions. Statistically, a randomly oriented oblate body with a given axis ratio is more likely than its prolate counterpart to yield a large rotational amplitude consistently during each revolution. It is apparent in **Figure 9** that the object exhibited consistently deep brightness minima. In this sense, we should assume that 'Oumuamua is a flattened, disk-like body, not an elongated, cigar-shaped one. Energy dissipation favors relaxation to the minimum energy (maximum moment of inertia) rotational state, which would work in favor of a prolate body shape, but the timescale for this relaxation depends on unknown physical parameters of the body and is suspected to be very long (Drahus et al. 2018).

**3.4.2. Other Interpretations.** It is possible that the light curve of 'Oumuamua could result from azimuthal albedo variations instead of from projected shape variations. In Solar System bodies, however, azimuthal albedo variations are almost always so small as to be immeasurable. The physical reason is that the surface material is homogenized, by both space weathering and gardening (the churning of exposed surface materials by micrometeorite bombardment). These processes, acting together or alone, render the surfaces of almost all asteroids and comets uniform in their scattering properties. The one notable exception to this is provided by Saturn's 1,500-km-diameter satellite Iapetus, which sports hemispheric ∼10:1 albedo variations. Iapetus is a special case, however, because the satellite is in a spin orbit resonance, exposing one hemisphere to the impact of debris from another Saturnian satellite while the other hemisphere survives unscathed (Tamayo et al. 2011). It is difficult to imagine how any comparable asymmetry could arise over the surface a body when free-floating in interstellar space. Therefore, although the possibility that the light curve of 'Oumuamua is caused by extreme azimuthal albedo variations cannot be formally rejected, it seems less plausible than an origin in the shape of the body.

**3.4.3. 2I/Borisov.** The optical cross section of 2I/Borisov was dominated by dust in the coma, preventing the separation of the signal from the underlying nucleus. For this reason, the rotational light curve could not be measured. Photometric variations in the coma instead provide a measure of the dust production rates in the object, subject to corrections for the changing viewing geometry. 2I/Borisov was observed over a wide range of phase angles, 40 deg $\lesssim \alpha \lesssim$ 90 deg, necessitating a large and correspondingly uncertain phase correction. Depending on the details of this correction, some observers (Jewitt & Luu 2019) reported a net increase in dust cross section on the approach to perihelion (commensurate with increasing gas production rates; Section 3.5), whereas others inferred steady fading (Hui et al. 2020).

## 3.5. Gas Production

The optical spectra of small solar system bodies are dominated by sunlight scattered from solid matter. At small heliocentric distances, typically ≤3 AU, gas can be detected through emission lines and bands caused by resonance fluorescence of sunlight. The most prominent cometary species are the radicals CN, $C_2$, $C_3$, and OH. Detection of gaseous molecules requires that observations be taken at longer wavelengths, in the IR and millimeter regimes.

**3.5.1. 1I/'Oumuamua.** No spectroscopic evidence for volatile outgassing was found in 'Oumuamua (Ye et al. 2017, Fitzsimmons et al. 2018, Trilling et al. 2018). We summarize the

**Table 3 Upper limits to gas production rates in 'Oumuamua**

| Species | Physical property | Value (mol $s^{-1}$) | Distance (AU) | Reference |
|---|---|---|---|---|
| CN | $Q$(CN) | $<2 \times 10^{22}$ | 1.4 | Ye et al. (2017) |
| $C_2$ | $Q(C_2)$ | $<4 \times 10^{22}$ | 1.4 | Ye et al. (2017) |
| $C_3$ | $Q(C_3)$ | $<2 \times 10^{21}$ | 1.4 | Ye et al. (2017) |
| OH | $Q$(OH) | $<1.7 \times 10^{27}$ | 1.8 | Park et al. (2018) |
| $CO_2$ | $Q(CO_2)$ | $<9 \times 10^{22}$ | 2.0 | Trilling et al. (2018) |
| CO[a] | $Q$(CO) | $<9 \times 10^{23}$ | 2.0 | Seligman et al. (2021) |

[a]Corrected from $Q(\mathrm{CO}) < 9 \times 10^{21}$ reported by Trilling et al. (2018).

reported upper limits to production rates, $Q$, in **Table 3**. The corresponding mass production rates are $\dot{M} = \mu m_{\mathrm{H}} Q$, where $\mu$ is the molecular weight of the species in question and $m_{\mathrm{H}}$ is the mass of the hydrogen atom. From the table, we compute limits for water, $\dot{M} \leq 30$ kg $s^{-1}$, and for CO, $\dot{M} < 0.04$ kg $s^{-1}$. As a comparison, peak production rates from comet C/1995 O1 (Hale–Bopp) were $3 \times 10^5$ kg $s^{-1}$ in water and $9 \times 10^4$ kg $s^{-1}$ in CO (Biver et al. 2002).

**3.5.2. 2I/Borisov.** In contrast, the spectrum of 2I/Borisov showed distinct gas emission bands rising above its dusty continuum, corresponding to the classical resonance fluorescence features observed in SPCs and LPCs. **Tables 4** and **5** summarize the spectroscopic results. The production rate data are also plotted in **Figure 11** as a function of the time of observation. The figure shows a relatively small variation in the production rates, reflecting the small range of heliocentric distances over which data were obtained.

The mass-dominant cometary volatile in SPCs and LPCs, $H_2O$, was measured systematically in 2I/Borisov by Xing et al. (2020). They obtained observations at six epochs before and after perihelion with the *Neil Gehrels Swift Observatory*'s Ultraviolet/Optical Telescope. These data

**Table 4 Production rates of CO, $H_2O$, and OH measured for 2I/Borisov[a]**

| Date | $r_{\mathrm{H}}$[b] (au) (AU) | Q($H_2O$) $10^{26}$ ($s^{-1}$) | Q(CO) $10^{26}$ ($s^{-1}$) | Q(OH) $10^{26}$ ($s^{-1}$) | Reference |
|---|---|---|---|---|---|
| 9/27/19 | 2.56 | <8.2 | | | Xing et al. (2020) |
| 10/2/19 | 2.50 | | | <0.2 | Opitom et al. (2019) |
| 10/11/19 | 2.38 | 6.3 ± 1.5 | | | McKay et al. (2020) |
| 10/13/19 | 2.36 | | | <0.2 | Opitom et al. (2019) |
| 11/1/19 | 2.17 | 7.0 ± 1.5 | | | Xing et al. (2020) |
| 12/1/19 | 2.01 | 10.7 ± 1.2 | | | Xing et al. (2020) |
| 12/3/19 | 2.01 | | 3.3 ± 0.8 | | Yang et al. (2021) |
| 12/11/19 | 2.01 | | 7.5 ± 2.3 | | Bodewits et al. (2020) |
| 12/15-16/19 | 2.02 | | 4.4 ± 0.7 | | Cordiner et al. (2020) |
| 12/19-22/19 | 2.03 | 4.9 ± 0.9 | 6.4 ± 1.4 | | Bodewits et al. (2020) |
| 12/21/19 | 2.03 | 4.9 ± 0.9 | | | Xing et al. (2020) |
| 12/30/19 | 2.07 | | 10.7 ± 6.4 | | Bodewits et al. (2020) |
| 1/13/20 | 2.16 | <5.6 | 8.7 ± 3.1 | | Bodewits et al. (2020) |
| 1/14/20 | 2.17 | <6.2 | | | Xing et al. (2020) |
| 2/17/20 | 2.54 | <2.3 | | | Xing et al. (2020) |

[a]Table adapted from Seligman et al. (2022).
[b]Heliocentric distance at observation.

**Table 5 Production rates of CN, $C_2$, and $C_3$ measured for 2I/Borisov[a]**

| Date | $r_H$[b] (au) (AU) | Q(CN) $10^{24}$ ($s^{-1}$) | Q($C_2$) $10^{24}$ ($s^{-1}$) | Q($C_3$) $10^{24}$ ($s^{-1}$) | Reference |
|---|---|---|---|---|---|
| 9/20/19 | 2.67 | 3.7 ± 0.4 | <4 | | Fitzsimmons et al. (2019) |
| 9/20/19 | 2.67 | <5 | <8 | | Kareta et al. (2020) |
| 10/1/19 | 2.50 | 1.1 ± 2.0 | <2.5 | | Kareta et al. (2020) |
| 10/1/19 | 2.51 | 1.8 ± 0.1 | <0.9 | <0.3 | Opitom et al. (2019) |
| 10/2/19 | 2.50 | 1.9 ± 0.1 | <0.6 | <0.2 | Opitom et al. (2019) |
| 10/9/19 | 2.41 | 1.59 ± 0.09 | <0.44 | | Kareta et al. (2020) |
| 10/10/19 | 2.39 | 1.69 ± 0.04 | <0.162 | | Kareta et al. (2020) |
| 10/13/19 | 2.36 | 2.1 ± 0.1 | <0.6 | <0.3 | Opitom et al. (2019) |
| 10/18/19 | 2.31 | 1.9 ± 0.6 | | | Opitom et al. (2019) |
| 10/20/19 | 2.29 | 1.6 ± 0.5 | | | Opitom et al. (2019) |
| 10/26/19 | 2.23 | 1.9 ± 0.3 | | | Kareta et al. (2020) |
| 10/31/19 | 2.18 | 2.0 ± 0.2 | | | Lin et al. (2020) |
| 11/4/19 | 2.15 | 2.4 ± 0.2 | 0.55 ± 0.04 | 0.03 ± 0.01 | Lin et al. (2020) |
| 11/10/19 | 2.12 | 1.9 ± 0.5 | | | Bannister et al. (2020) |
| 11/14/19 | 2.09 | 1.8 ± 0.2 | 1.1 | | Bannister et al. (2020) |
| 11/17/19 | 2.08 | 1.9 ± 0.5 | | | Bannister et al. (2020) |
| 11/25/19 | 2.04 | 1.6 ± 0.5 | | | Bannister et al. (2020) |
| 11/26/19 | 2.04 | 1.8 ± 0.2 | | | Bannister et al. (2020) |
| 11/26/19 | 2.04 | 1.5 ± 0.5 | 1.1 | | Bannister et al. (2020) |
| 11/30/19 | 2.01 | 3.36 ± 0.25 | 1.82 ± 0.6 | 0.197 ± 0.052 | Aravind et al. (2021) |
| 12/22/19 | 2.03 | 6.68 ± 0.27 | 2.3 ± 0.82 | 0.714 ± 0.074 | Aravind et al. (2021) |

[a]Table adapted from Seligman et al. (2022).
[b]Heliocentric distance at observation.

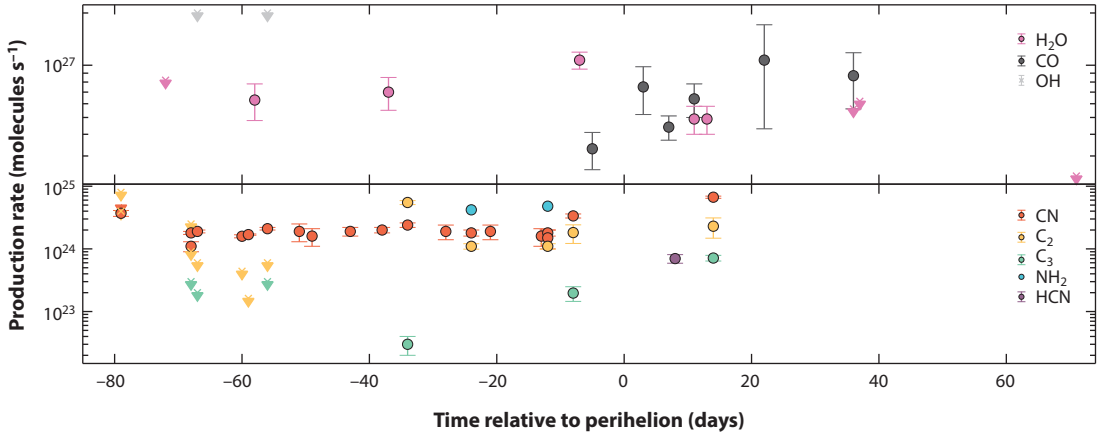


**Figure 11**

Time dependence of 2I/Borisov production rates. The top panel shows production rates of $H_2O$, CO, and OH (**Table 4**), and the bottom panel shows production rates of CN, $C_2$, $C_3$, $NH_2$, and HCN (**Table 5**). Figure adapted from Seligman et al. (2022).

revealed a water production rate peaking near $Q(H_2O) = (10.7 \pm 1.2) \times 10^{26}$ s$^{-1}$ at perihelion, corresponding to a mass production rate of $\dot{M}(H_2O) = 32$ kg s$^{-1}$. Adopting a nominal equilibrium sublimation rate of water ice at 2 AU equal to $f_s = 5 \times 10^{-5}$ kg m$^{-2}$ s$^{-1}$ (obtained from solution of the energy balance Equation 3), the required area of exposed and sublimating water ice is $C = \dot{M}(H_2O)/f_s \sim 0.64$ km$^2$. This surface area corresponds to that of a circle with radius $r_n = (C/\pi)^{1/2} \sim 0.45$ km. This sublimation radius lies close to the nominal 0.4-km nucleus radius and to the upper limit (0.5 km) obtained by Jewitt et al. (2020b) in an independent calculation. These two independent estimates both corroborate each other and imply that the surface of 2I/Borisov had a large active fraction, $f_A \sim 1$. This, in turn, matches measurements showing that SPC nuclei of size comparable with 2I/Borisov typically have $f_A \sim 1$ (Jewitt 2021).

2I/Borisov was also a productive source of carbon monoxide, CO, with a production rate ratio measured on multiple dates to be $Q(CO)/Q(H_2O) = 0.7 \pm 0.3$ (Cordiner et al. 2020), and even >1 as in **Table 4** (Bodewits et al. 2020). This is substantially higher than mean values $Q(CO)/Q(H_2O) = 0.04$ in Solar System comets at distances $\lesssim$2.5 AU (Bockelée-Morvan & Biver 2017, McKay et al. 2019). The high relative abundance of CO implies low temperature formation of 2I/Borisov in order to trap the CO, presumably in the outer regions of a protoplanetary disk. It also implies low-temperature storage in order to retain the CO against sublimation since the formation epoch (see Section 4.6).

## 4. PHYSICAL MODELS

A central puzzle is that 1I/'Oumuamua showed no visible coma in deep composite images, and yet it had a nongravitational acceleration of 30$\sigma$ significance. These two observations have prompted theories, from the mundane to the fantastical, regarding the provenance of the object. In comparison, the properties of 2I/Borisov were closer to those observed in numerous Solar System comets.

### 4.1. Recoil from Outgassing

Nongravitational accelerations in Solar System comets are caused by recoil in response to the sublimation of surface ice in the heat of the Sun and the subsequent anisotropic mass ejection. The recoil force may be written as $k_R \dot{M} V_s$, where $\dot{M}$ is the sublimation rate, $V_s$ is the speed of the ejected material, and $0 \leq k_R \leq 1$ is a dimensionless constant representing the degree of anisotropy of the outflow. For perfectly isotropic flow, $k_R = 0$, whereas for perfectly collimated outflow, $k_R = 1$. Newton's law applied to a body of spherical-equivalent radius $r_n$ and bulk density $\rho_n$ then gives,

$$\dot{M} = \left(\frac{4\pi \rho_n r_n^3}{3}\right)\left(\frac{\alpha_{ng}(1)}{k_R V_s}\right), \qquad 2.$$

for the mass-loss rate needed to generate the acceleration, $\alpha_{ng}(1)$.

Measurements of comets show that sublimation proceeds mostly from the hot dayside of the nucleus. Correspondingly, the recoil force acts primarily in the radial direction away from the Sun (i.e., along $A_1$), as can be seen in **Table 1**. The magnitude of $k_R$ has only been determined with confidence for the SPC 67P/Churyumov–Gerasimenko at $k_R = 0.5$ (Jewitt et al. 2020b) and is otherwise not well known. We adopt this value here. The speed of sublimated gas is close to the thermal velocity of gas molecules at the sublimation temperature of ice. For water ice at $r_H \lesssim 2$ AU, this is $T \sim 200$ K, giving $V_s \sim 500$ m s$^{-1}$, a value we adopt throughout. The average density of Solar System cometary nuclei is $\rho_n \sim 500$ kg m$^{-3}$ (Groussin et al. 2019), which we also adopt here. Substitution into Equation 2, with our nominal spherical-equivalent radius

estimate for 'Oumuamua $r_n = 80$ m, gives $\dot{M} \sim 24$ kg s$^{-1}$. For the larger nucleus of 2I/Borisov, with $200 \leq r_n \leq 500$ m, mass loss rates $\dot{M} = 400$ to 6,000 kg s$^{-1}$ (scaled to 1 AU) are needed to account for $\alpha_{ng}(1)$. Can these rates be supplied by sublimation of cometary volatiles?

The equilibrium rate of sublimation of a volatile surface exposed to the Sun is given by solutions to the following equation:

$$\left(\frac{(1-A)\,L_\odot}{4\pi r_H^2}\right)\cos(\theta) = \varepsilon\sigma T^4 + Hf_s(T) + C(T). \quad 3.$$

Here, $L_\odot$ (W) is the luminosity of the Sun, $r_H$ (m) the heliocentric distance, $A$ and $\varepsilon$ are the Bond albedo and thermal emissivity of the surface, $\sigma$ (W m$^{-2}$ K$^{-4}$) is the Stefan–Boltzmann constant, $T$ (K) is the surface temperature, $H$ (J kg$^{-1}$) is the latent heat of sublimation, and $f_s(T)$ (kg m$^{-2}$ s$^{-1}$) is the specific sublimation rate. The angle $\theta$ is the angle between the surface normal and the direction to the Sun. The term on the left-hand side represents the absorbed solar power. The terms on the right-hand side account for the thermal radiation, the breaking of hydrogen bonds in sublimation, and conduction into the interior, respectively. The surface materials on Solar System bodies tend to be porous and have low thermal conductivity, justifying the neglect of the conduction term $C(T)$ in most cases. The latent heats of water and CO ice are $H = 2.8 \times 10^6$ J kg$^{-1}$ and $H = 2 \times 10^5$ J kg$^{-1}$, respectively. Equation 3 cannot be solved alone, and the Clausius–Clapeyron equation is commonly used in addition to represent the temperature dependence of the sublimation phase boundary in $f_s(T)$. Furthermore, the equation must be solved for a surface divided into elements, each with its own angle, $\theta$, to the solar direction. The averaged value of $\cos(\theta)$ is as follows: $\overline{\cos(\theta)} = 1$ for a flat surface oriented normal to the Sun, $\overline{\cos(\theta)} = 1/2$ for a spherical body sublimating only from the Sun-facing hemisphere, and $\overline{\cos(\theta)} = 1/4$ for a uniformly sublimating sphere. $\overline{\cos(\theta)} = 1$ represents the highest possible temperature, corresponding to the noon-day equatorial Sun, whereas $\overline{\cos(\theta)} = 1/4$ corresponds to the lowest possible temperature on a sublimating, isothermal sphere. The optical properties $A$ and $\varepsilon$ are generally not well constrained, but Equation 3 is insensitive to both provided $A \ll 1$ and $\varepsilon \gg 0$. Here, we assume $A = 0$ and $\varepsilon = 0.9$.

We adopt a nominal reference distance of $r_H = 1$ AU and assume that sublimation occurs from the Sun-facing hemisphere of a spherical body [i.e., $\overline{\cos(\theta)} = 1/2$]. Under these assumptions, Equation 3 gives $f_s(H_2O) = 2.2 \times 10^{-4}$ kg m$^{-2}$ s$^{-1}$ and $f_s(CO) = 2.3 \times 10^{-3}$ kg m$^{-2}$ s$^{-1}$ for the more volatile substance. We emphasize that these values are strictly valid only for sublimation at the surface. A volatile that is protected from direct heat by an overlying layer of less volatile material (as is likely to be the case for highly volatile CO, for example) will sublimate at a smaller but much more model-dependent rate. Production rates of water in Solar System comets vary approximately as $r_H^{-2}$ out to $r_H \sim 2$ AU. Production rates of CO vary similarly, but out to $r_H \sim 50$ AU. This is due to the exponential rise in the sublimation term in Equation 3, which is only in competition with the radiation term with $\sim T^4$ dependence. The model mass-loss rate, $\dot{M}$, is given by $\dot{M} = 2\pi r_n^2 f_s f_A$, where $f_A$ is the fraction of the nucleus surface from which ice sublimates. By substituting this into Equation 2, the expected nongravitational acceleration, $\alpha_{ng}$ for each volatile may be calculated. As shown in **Figure 12**, the active fraction on SPCs shows a clear trend with the nucleus radius (Jewitt 2021), represented by a best-fit power law,

$$f_A \simeq 0.1\, r_n^{-2}, \quad 4.$$

for $r_n \gtrsim 0.3$ km (and $f_A = 1$ otherwise). This trend is likely produced, at least in part, by observational bias, stemming from the fact that small nuclei with small active fractions are intrinsically faint and less likely to be discovered in flux-limited surveys. We plot and label the estimated radii of 1I and 2I in **Figure 12**. Both objects are small enough to suggest large active fractions, $f_A \sim 1$, by analogy with the SPCs, and we adopt $f_A = 1$ here.

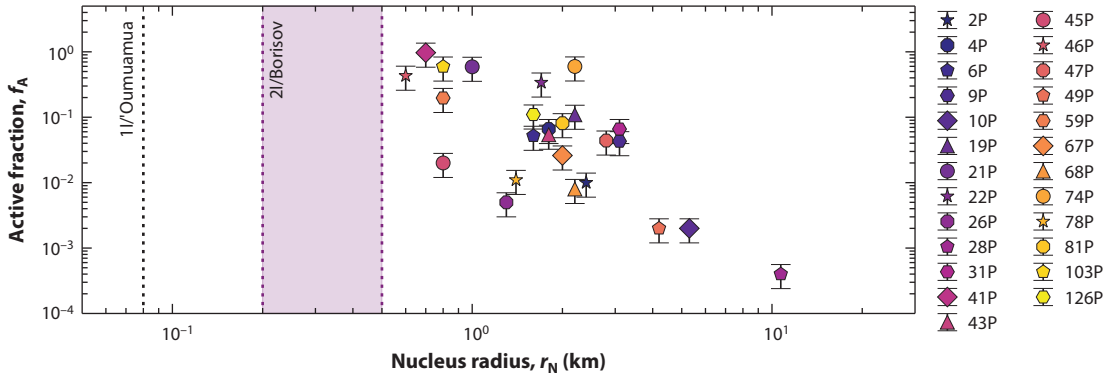


**Figure 12**

Active sublimation surface fractions measured in Solar System comets. Figure adapted from Jewitt (2021, their figure 2).

In the case of 1I/'Oumuamua, there are two immediate problems. The first concerns the identity of the sublimating volatile. Water ice sublimates too slowly at 1 AU to supply the $\dot{M} = 24\,\mathrm{kg\,s^{-1}}$ needed to provide $\alpha_{ng}(1)$ as originally pointed out in an unrefereed preprint by Sekanina (2019b). Instead, supervolatile ices (e.g., $H_2$, $N_2$, CO, Ne, and Ar) sublimating in equilibrium with sunlight are required to generate sufficient recoil, as a result of their relatively small latent heats of sublimation. The noble gases have low abundance and are unlikely sources of activity. Seligman & Laughlin (2020) proposed that 1I/'Oumuamua was composed of solid hydrogen, $H_2$, presumably formed in a prestellar core of a giant molecular cloud (GMC) that failed to form a star (cf. Hoang & Loeb 2020, Levine & Laughlin 2021). However, uncommonly frigid temperatures ($T < 6$ K) are needed to accrete and retain solid $H_2$, and the survival of such a volatile object in the open ISM is in doubt.

Next, Desch & Jackson (2021) and Jackson & Desch (2021) proposed that sublimating $N_2$ could be the cause of the acceleration. Nitrogen has the advantage of being spectroscopically inert, consistent with its nondetection in 'Oumuamua. However, in the Solar System, large nitrogen ice reservoirs are known to exist only on the surfaces of large, thermally differentiated KBOs, with Pluto providing the premier example. It is unlikely that sufficient exposed solid nitrogen exists on differentiated extrasolar KBOs to act as a galaxy-wide supply of 1I/'Oumuamua-like bodies (Levine et al. 2021).

Finally, Seligman et al. (2021) suggested that carbon monoxide (CO) sublimation could supply the recoil acceleration. Equilibrium hemispheric sublimation of CO from an 80-m-radius body at 1 AU is indeed sufficient to provide $\dot{M} = 24$ kg s$^{-1}$ needed to accelerate 'Oumuamua. Furthermore, CO is an abundant and observationally well-established volatile in Solar System comets; its existence in 'Oumuamua would not be surprising. Unfortunately, empirical limits to CO production in 'Oumuamua [Trilling et al. 2018; even when corrected for a numerical error to $Q_{CO} = 9 \times 10^{23}$ s$^{-1}$ ($\sim$0.04 kg s$^{-1}$) by Seligman et al. 2021; **Table 4**], are three orders of magnitude too small for CO to account for the nongravitational acceleration. The identity of a possible gaseous driver of the nongravitational acceleration thus remains unresolved.

The second problem with outgassing as an explanation of the nongravitational acceleration of 'Oumuamua is that no dust coma was detected. Gas and dust mass production rates are comparable in typical comets, but the ejected dust typically dominates the optical appearance. This is because the dust has a much larger scattering cross section per unit mass of material than does the gas, which is only rendered visible through resonance fluorescence. Therefore, if sublimation caused

the nongravitational acceleration of 1I/'Oumuamua, it is particularly puzzling that no comet-like, dusty coma was evident even in the deepest images. The empirical limits on the production rate of micron-sized particles [$<0.2$–$2 \times 10^{-3}$ kg s$^{-1}$ (Jewitt et al. 2017, Meech et al. 2017)] are orders of magnitude smaller than required to supply the nongravitational acceleration.

A possible solution to this problem is that dust could be hidden from view given a sufficiently large effective particle radius (Micheli et al. 2018). The cross section per unit mass of a collection of spheres with radius, $a$, varies as $\propto 1/a$. Millimeter-sized particles in 'Oumuamua would present $10^{-3}$ of the cross section of an equal mass of micron-sized particles. Consequently, they would be $10^3$ times fainter in scattered light, perhaps allowing them to have escaped detection. This suggestion is ad hoc in the specific case of 'Oumuamua, but measurements of some weakly active comets (e.g., Ishiguro et al. 2007) and active asteroids (Jewitt & Hsieh 2022) indeed indicate mean particle radii of $10^2$ μm and greater. The physical explanation for this is not well understood, but a possible cause is that interparticle cohesion (which itself varies as $1/a$) prevents small particles from escaping into the coma under the action of weak gas drag, leaving only the large particles to be ejected (Skorov & Blum 2012).

Another possibility is that 1I/'Oumuamua outgassed through a porous mantle having enough strength to resist the expulsion of dust particles. Again, this explanation is both ad hoc and untestable. As a result, a consistent explanation of the origin of 'Oumuamua's nongravitational acceleration by outgassing has not been reached, and alternative explanations resting on the action of radiation pressure have been proposed (Section 4.2).

The case of 2I/Borisov is more clear-cut. We possess independent estimates of the nucleus radius ($200 \leq r_n \leq 500$ m; Jewitt et al. 2020a), the nongravitational acceleration (**Table 1**), and the mass-loss rate in gas (**Table 4**). The latter is ∼80 kg s$^{-1}$ at 2 AU or $\dot{M} \sim 320$ kg s$^{-1}$ when scaled to 1 AU by the inverse square law. Using these values to solve Equation 2 for the nucleus density then gives $100 \leq \rho_n \leq 1{,}600$ kg m$^{-3}$, which is a plausible range that brackets the nominal $\rho_n = 500$ kg m$^{-3}$ density of Solar System comets (Groussin et al. 2019). Ultralow densities like that posited for 'Oumuamua (Section 4.2) are specifically excluded from the allowable range of solutions for 2I/Borisov. The coma morphology is consistent with a dust differential power-law-size distribution index $-3.5$ and an effective mean particle size $a \gtrsim 100$ μm (Jewitt & Luu 2019, Hui et al. 2020, Kim et al. 2020), suggesting the role of small particle sticking as posited for 1I/'Oumuamua.

## 4.2. Radiation Pressure: Fractal Bodies

Radiation pressure offers an entirely different interpretation of the nongravitational acceleration of 1I/'Oumuamua. At 1 AU, the radiative pressure is $F_\odot/c$, where $F_\odot = 1{,}360$ W m$^{-2}$ is the solar constant and $c = 3 \times 10^8$ m s$^{-1}$ is the speed of light. The force on a spherical body of radius $r_n$ is then $\pi F_\odot r_n^2/c$ and, by Newton's law, the density required to account for the measured nongravitational acceleration may be written as

$$\rho_n = \left(\frac{3}{4r_n}\right)\left(\frac{F_\odot}{c\alpha_{ng}(1)}\right). \quad 5.$$

By substitution of $\alpha_{ng}(1)$ for 'Oumuamua, we find that $\rho_n \sim 0.01(100/r_n)$ kg m$^{-3}$. This is two orders of magnitude less dense than air and implies a highly porous structure. For comparison, the least dense artificial solid is aerographite with $\rho = 0.2$ kg m$^{-3}$ (Mecklenburg et al. 2012). Built of a complex assemblage of thin carbon sheets and tubes, aerographite is still an order of magnitude denser than required of 'Oumuamua by Equation 5.

Could such a low-density material form naturally? One suggestion is that 'Oumuamua could have a fractal structure produced by ballistic cluster–cluster aggregation (BCCA) in an ultralow

energy protoplanetary disk environment (Moro-Martín 2019). The mass of a fractal, $m_f$, varies with its size, $a_f$, as $m_f \propto a_f^D$, and the density scales as $\rho_f \propto a_f^{D-3}$, where $D$ is the fractal dimension. Therefore, smaller values of $D$ correspond to less dense, more open, and even "stringy" structures enveloping large void spaces.

Fractal aggregates have been investigated in the context of planetary accretion, where they offer several attractive features. These include tight dynamical coupling with the gas, providing a way to overcome the radial drift, fragmentation, and bouncing barriers to the growth of large bodies (Meakin & Donn 1988, Suyama et al. 2008, Garcia & Gonzalez 2020). Tiny (0.1 μm?) monomers would be well coupled to the disk gas and therefore would collide gently, at speeds set initially by Brownian motion. In BCCA, comparably sized clusters collide and stick, producing larger clusters of lower density. The fractal dimension in BCCA is $D \sim 2$, meaning that the density varies as $\rho_f \propto a_f^{-1}$. As the aggregate sizes grow to $a_f \sim 1$ to 10 mm, numerical models show that the density reaches a minimum value $\rho_f \sim 10^{-2}$ kg m$^{-3}$ (i.e., comparable with that required of 1I/'Oumuamua by Equation 5) (Kataoka et al. 2013). At larger sizes, the particle clusters are compressed, first by about an order of magnitude due to ram pressure from the surrounding gas and then to comet-like densities at size scales of $a_f \gtrsim 10^2$ m, by gravitational self-compression. The particles in a fractal structure are held together by incredibly weak van der Waals forces but, counter-intuitively, even with densities as small as $\sim 10^{-2}$ kg m$^{-3}$, fractal structures could survive the stresses induced by rotation and Solar tides (Flekkøy et al. 2019). Indeed, aerographite has a tensile strength of $\sim 10^3$ N m$^{-2}$ (Mecklenburg et al. 2012).

There is some evidence for fractal structure in comets, but only on very small spatial scales. Submillimeter aggregates gently collected from the coma of 67P/Churyumov-Gerasimenko had densities of $<1$ kg m$^{-3}$ (Fulle et al. 2015) and fractal dimensions of $D = 1.7 \pm 0.1$ (Mannel et al. 2016). However, this density is still larger, by a factor of $10^2$, than the 0.01 kg m$^{-3}$ density implied by Equation 5 for 'Oumuamua. Furthermore, although some individual submillimeter particles in the nucleus of 67P show low densities and fractal structure, a majority do not. The bulk density of the nucleus is a much more compact $\rho_n \sim 500$ kg m$^{-3}$ (Groussin et al. 2019).

There are no known ultralow density bodies of significant size in the Solar System, but this could be a selection effect; even if the Solar System formed with an abundance of gently agglomerated, ultralow-density bodies, it is unlikely that any would survive today. Compression or destruction by impact in later, more energetic phases of planetary accretion would erase any evidence of their existence. Only fractal bodies ejected early to the collisionless environment of interstellar space would have had a chance to survive.

As a novel caveat to this idea, Luu et al. (2020) suggested that fractal bodies might actively form in the comae of other comets, as particles lifted from the surface collide and stick to form "dust bunny" aggregates. Although most cometary fragments appear short-lived, in this scenario we should be able to observe cometary fragments that are progressively accelerated into hyperbolic orbits.

### 4.3. Radiation Pressure: Membrane

The measured acceleration of 'Oumuamua, if due to radiation pressure, could instead imply a thin sheet geometry with a low column density, $\Sigma$ (kg m$^{-2}$), given by

$$\Sigma = \left( \frac{F_\odot}{c\, \alpha_{ng}(1)} \right). \quad 6.$$

Substitution for the case of 'Oumuamua gives $\Sigma \sim 0.8$ kg m$^{-2}$, a value that is more typical of a thin sheet of cardboard (density of $\sim 10^3$ kg m$^{-3}$, thickness of $\sim 10^{-3}$ m) than of any natural, macroscopic object.

Bialy & Loeb (2018) suggested that 'Oumuamua could be a razor-thin sheet or membrane, perhaps akin to a light-sail. Such a structure would have a column density small enough to be accelerated by radiation pressure and, with a dimension $r_n \sim 100$ m, the corresponding sheet mass would be $r_n^2 \Sigma \sim 10^4$ kg, or smaller if the albedo is higher. Because the orbit of 'Oumuamua is gravitationally unbound, they inferred that 'Oumuamua could be the manufactured product of an alien civilization. Active radio signals transmitted from 'Oumuamua were sought but not detected (Enriquez et al. 2018, Tingay et al. 2018, Harp et al. 2019).

The alien membrane hypothesis is consistent with the existence of nongravitational acceleration without detectable mass loss, provided the membrane maintains an orientation nearly perpendicular to sunlight. It is also qualitatively consistent with 'Oumuamua's extreme light curve, albeit with a low (∼1%) probability for having the orientation needed to generate the observed large amplitude (Zhou et al. 2022). The alien membrane hypothesis is highly questionable on other grounds, however. For example, 'Oumuamua cannot be a probe targeted at Earth because it missed by ∼40 million km; intelligent aliens could surely do better. Could 'Oumuamua instead be a piece of alien space trash? If so, it is difficult to see why an intelligent civilization would flood the galaxy with $10^{25}$ or $10^{26}$ (Section 5.1) pieces of 100-m-scale Mylar-like debris.

### 4.4. Stability Against Spin-Up Destruction

Models of the unexpected properties of 1I/'Oumuamua thus require either strained explanations in terms of the outgassing of unseen volatiles or explanations invoking material of such low column density that radiation pressure has a strong effect. Whichever model applies, the strong nongravitational acceleration of this object implies that substantial torques should have modified the spin of the nucleus, potentially driving it to rotational instability (Rafikov 2018a).

The nuclei of SPCs show clear evidence for the action of outgassing torques, in the form of small changes in the rotation period per orbit, $\Delta P$ (Kokotanekova et al. 2018). When sustained over sufficiently long times, these outgassing torques can drive comets to rotational instability, in which centripetal forces exceed those of gravity and material cohesion acting to bind the nucleus. The result is nucleus breakup or disintegration, widely observed in both SPCs (Jewitt 2021) and LPCs (Jewitt 2022).

Empirically, the timescale for changing the nucleus spin can be computed from

$$\tau_S = \left( \frac{P}{\Delta P} P_K \right), \qquad 7.$$

where $P$ is the measured rotational period, $\Delta P$ is the change in rotational period per orbit, and $P_K$ is the Keplerian orbital period. **Table 6** lists measurements of $\Delta P$, whereas **Figure 13** shows $\tau_S$ as a function of nucleus radius for the nuclei of SPCs having perihelion distance $1 \leq q \leq 2$ AU. To a good level of approximation, the timescale is represented by

$$\tau_S \simeq 100\, r_n^2 \text{ (years)}, \qquad 8.$$

where $r_n$ is the nucleus radius expressed in kilometers. Equation 8 is shown in the figure as a dashed line.

The small nuclei of 1I/'Oumuamua and 2I/Borisov, both indicated in **Figure 13**, have very short spin-up times, with that for 'Oumuamua being <1 year. In fact, 1I/'Oumuamua should spin up even more quickly than indicated by Equation 8, because its small perihelion distance would induce larger outgassing rates than in the comparison comet population and because of its extreme aspect ratio. The latter would give a longer lever arm than for a more nearly spherical nucleus. Based on these considerations, Rafikov (2018b) argued that the lack of steady spin-up and constant periodicity in the light curve implied that outgassing could not explain the anomalous acceleration.

**Table 6 Empirical spin-changes of short-period comet nuclei[a]**

| Comet Name | $q$[b] (AU) | $P_K$[c] (years) | $P$[d] (h) | $\Delta P$[e] (min) | Reference |
|---|---|---|---|---|---|
| 2P/Encke | 0.337 | 3.30 | 11.0 | 4 | Roth et al. (2018) |
| 9P/Tempel | 1.542 | 5.58 | 40.9 | 13.5 | Gicquel et al. (2012) |
| 10P/Tempel | 1.423 | 5.37 | 8.9 | 0.27 | Wilson et al. (2017) |
| 14P/Wolf | 2.729 | 8.80 | 9.0 | <4.2 | Fernández et al. (2013) |
| 19P/Borrelly | 1.358 | 6.86 | 29.0 | 20 | Maquet et al. (2012) |
| 41P/TGK | 1.046 | 5.42 | 34.8 | 1560 | Combi et al. (2020) |
| 46P/Wirtanen | 1.055 | 5.44 | 9.15 | 12 | Combi et al. (2020) |
| | | | | | Farnham et al. (2021) |
| 49P/Arend–Rigaux | 1.343 | 6.62 | 13.0 | <0.23 | Eisner et al. (2017) |
| 67P/C-G | 1.244 | 6.45 | 12.0 | 21 | Biver et al. (2019) |
| 103P/Hartley | 1.058 | 6.46 | 18.2 | 120 | Drahus et al. (2011) |
| | | | | | Combi et al. (2020) |
| 143P/Kowal–Mrkos | 2.542 | 8.90 | 17.0 | <6.6 | Jewitt et al. (2003) |
| 162P/Siding Spring | 1.232 | 5.30 | 33.0 | <25 | Fernández et al. (2013) |

[a]Table adapted from Jewitt (2021).
[b]Perihelion.
[c]Keplerian orbital period.
[d]Nucleus spin period.
[e]Measured change in nuclear spin period over the course of 1 orbit (Kokotanekova et al. 2018).

**Figure 14** shows the phased light curve of 'Oumuamua with photometric data obtained from only one telescope and presented by Drahus et al. (2018). The light curve is highly—but not completely—repetitive. For example, differences at the ~10% level are evident near phase = 0.01 and 0.35. If these differences are not due to measurement error, they could indicate a slightly excited or "tumbling" rotational state, which Drahus et al. (2018) interpreted as the result of an ancient collision in the protoplanetary disk of another star. Rotation can also be excited contemporaneously by mass loss and other torques.

Belton et al. (2018), Drahus et al. (2018), and Fraser et al. (2018) searched for periodicities in the composite light curve, after correcting the data for the changing phase angle and distance to

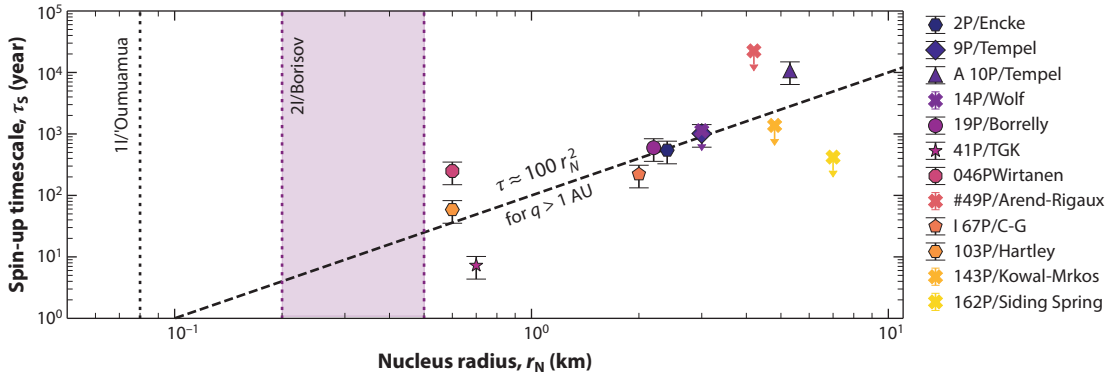


**Figure 13**

Spin-up timescales measured in Solar System comets. Equation 8 is shown as a dashed line. Figure adapted from Jewitt (2021, figure 1).

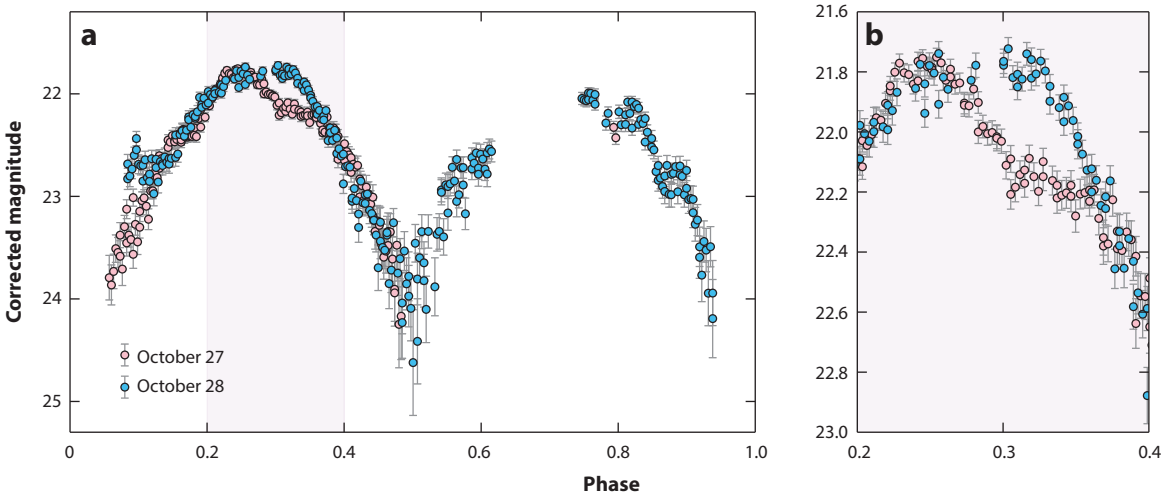


**Figure 14**

(*a*) Phased light curve data from 1I/'Oumuamua showing small differences between measurements three rotations apart, from UT October 27 (*pink circles*) and October 28, 2017 (*blue circles*). The data are phase folded at a period of 7.5483 h. (*b*) Zoom view of the region near phase 0.3 to show differences in the brightness. Data taken from Drahus et al. (2018).

'Oumuamua and for the use of different filters by different observers. An analysis by Belton et al. (2018) identified dominant periodic signals at 8.67 ± 0.34 and 3.74 ± 0.11 h, which is consistent with a single rigidly rotating and precessing nucleus, and these authors found no evidence for the action of torques on the rotation of 1I/'Oumuamua.

However, the Belton et al. (2018) analysis assumes a simple decomposition into discrete frequencies, potentially concealing evidence for the action of torques. Flekkøy et al. (2019) noticed that reported rotation periods of 1I/'Oumuamua increased linearly from 7.3 h to 8.2 h over the 3-day period UT October 26–29, 2017, corresponding to a spin-change timescale $\tau_S = P/\Delta P \sim 26$ days. This is broadly consistent with both the spin-up timescale for radiation torques [the YORP (Yarkovsky–O'Keefe–Radzievskii–Paddack) torque; Vokrouhlický et al. 2015] and for an ultralow-density ($10^{-2}$ kg m$^{-3}$) body only 80 m in radius. It is also consistent with the outgassing torque timescale computed from Equation 8 if the density is comet-like. Taylor et al. (2022) reported a 0.21-h decrease in the spin period between October and November, which is consistent with outgassing-induced torques. An independent analysis revealed that the addition of a torque significantly improves the fit to the light curve Mashchenko (2019). Furthermore, the best-fit moment arm for the torque ($k_T = 0.0046$) is similar to the median moment arm measured in SPCs ($k_T = 0.007$; (Jewitt 2021). (The same study also revealed that an oblate body shape is more likely than a prolate one).

Although different in detail, the Flekkøy et al. (2019) and Mashchenko (2019) studies still reveal fractional changes in the rotation period of order unity on timescales of ∼1 month, leaving it unclear how to reconcile the survival of the nucleus against rotational disruption with the large nongravitational acceleration. Point-source outgassing from the subsolar point would eliminate secular spin-up (Seligman et al. 2019), but this pathological geometry does not occur on the known comets. Likewise, a symmetric elongated body with jets uniformly covering the illuminated surface can produce stable spin dynamics (Seligman et al. 2021) but, again, this would be unlike outgassing from any of the known comets.

**Yarkovsky–O'Keefe–Radzievskii–Paddack (YORP):** energy absorbed by a body is reradiated anisotropically, exerting a weak torque (the "YORP torque")

One intriguing possibility is that 'Oumuamua did rotationally disrupt from outgassing torques near perihelion and that the body observed in 2017 is merely the remnant of a rotationally disrupted interstellar precursor nucleus that did not survive perihelion (Sekanina 2019a). The drifting spin period reported in figure 1 of Flekkøy et al. (2019), when extrapolated backward, reaches zero in early October, a few weeks after perihelion (Sekanina 2019a). Furthermore, this possibility is consistent with the observed disintegration of the nuclei of LPCs, a likely result of rotational instability when near the Sun (Jewitt 2022). Such rotational disintegration occurs preferentially in sub-kilometer nuclei with perihelia <1 AU; both conditions (radius ∼0.08 km, perihelion 0.25 AU) apply to 'Oumuamua. Residual outgassing from volatiles exposed by the breakup could further modify the rotation, and provide the nongravitational acceleration.

2I/Borisov, with its larger nucleus and perihelion distance, is less susceptible to rotational breakup, for which the timescale (Equation 8) is $4 \leq \tau_S \leq 25$ years. It did, however, release several fragments (**Figure 8**), possibly under the influence of nucleus rotation.

## 4.5. Tidal Disruption and Ejection

Comets in the Solar System are occasionally tidally disrupted when passing within the Roche lobe of the Sun or a giant planet. The most famous and best-studied example is that of the kilometer-sized, periodic comet P/Shoemaker-Levy 9 (1993 F2, "SL9"), which disrupted upon passing Jupiter at 1.6 times the planetary radius in 1992 (Weaver et al. 1995). The example provided by SL9 motivated Raymond et al. (2018) to consider 'Oumuamua as a tidally shredded fragment of a precursor cometary body from the protoplanetary disk of another star. They obtained an estimate of the fractional disruption rate of ejected bodies in the range of $10^{-3}$ to $10^{-2}$, although this number sensitively depends on the model assumptions. They also pointed out that a majority of disrupted fragments would be devolatilized by subsequent close approaches to the host star prior to escape (further investigated in Raymond et al. 2020). The fragment shapes produced by tidal disruption, subject to assumptions about the stellar impact parameter, rubble-pile structure, internal friction, and more, are prolate and can be as elongated as suggested by the light curve of 'Oumuamua (Zhang & Lin 2020). However, the galactic rates at which cometary disruptions and ejections occur, given the many unknowns, are highly uncertain.

Other potential sources of tidal fragments exist, including post-main-sequence stars (Hansen & Zuckerman 2017, Katz 2018, Rafikov 2018a), close stellar flybys in clusters (Pfalzner et al. 2021), and circumbinary systems (Ćuk 2018, Jackson et al. 2018). Childs & Martin (2022) argued that misaligned circumbinary disks are particularly efficient progenitors of interstellar asteroids, specifically of objects that are close enough to have lost their volatiles.

In addition to being tidally shredded, an object must be ejected from the gravitational control of its host star if it is to join the interstellar rank. In a given planetary system, the ejection efficiency depends on the stellar mass, $M_\star$, and on the distance, $a_P$, size, $R_P$, and mass, $M_P$, of the scattering planet. The distance and mass of the star set the Keplerian velocity, $V_K = (GM_\star/a_P)^{1/2}$. The size and mass of the planet set the escape velocity from the surface of planet, $V_e = (2GM_P/R_P)^{1/2}$. The escape velocity is a reasonable approximation for the maximum velocity that can be imparted in a scattering event.

A useful parameter to quantify the efficiency of ejection for any given perturber is the Safronov number, $\Theta = V_e^2/(2V_K^2)$ or, equivalently,

$$\Theta = \left(\frac{a_P}{R_P}\right)\left(\frac{M_P}{M_*}\right). \quad 9.$$

To a very good approximation, only planets with $\Theta > 1$ can eject objects via scattering. In the modern-day Solar System, the terrestrial planets have $\Theta < 1$ but all four giant planets satisfy

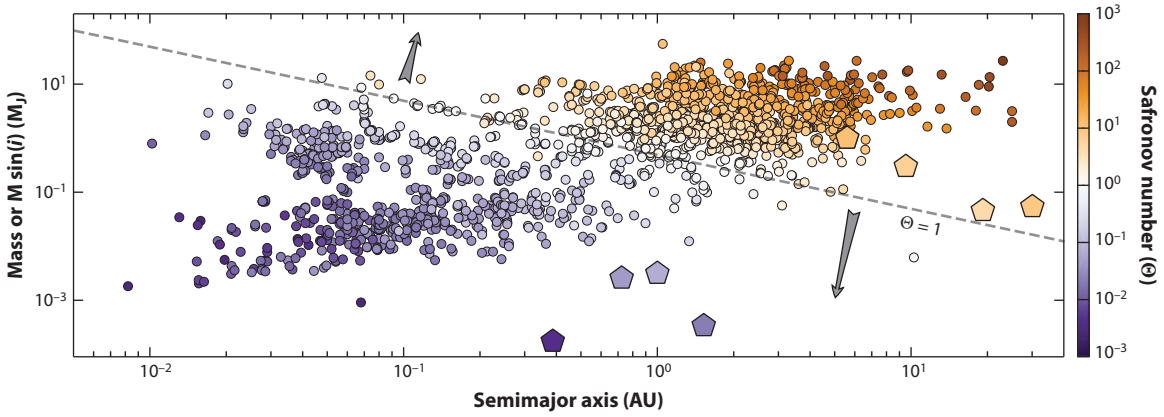


**Figure 15**

Safronov number (color coded) for the known exoplanets showing that those with $\Theta > 1$ are preferentially located in the outer regions of their systems (cf. Laughlin & Batygin 2017). Large pentagonal symbols show Solar System planets. The illustrative dashed line shows $\Theta = 1$, for a Jupiter-radius planet orbiting a solar mass star. For the most part, planets above the line are capable of ejecting comets to the interstellar medium, whereas those below it are not.

$\Theta > 1$ and are capable of ejecting comets into the ISM. The mass of material that can be ejected depends on the details of the planet–disk interaction. Importantly, for all planets in which $\Theta > 1$, larger values do not necessarily imply that the planet ejected more debris. For instance, Jupiter has a much higher mass than Neptune, and naively one would imagine that it dominated the cometary ejection in the Solar System. However, Neptune migrated over a larger range of distances than did Jupiter, providing it with access to a larger mass of nearby cometesimals. To complicate matters further, the density of the disk near Neptune was smaller than that for Jupiter. Hahn & Malhotra (1999) modeled this process and found that the Oort cloud emplacement efficiency is broadly distributed across the Jupiter to Neptune region.

In **Figure 15**, we show the Safronov number for currently confirmed extrasolar planets (cf. Laughlin & Batygin 2017, their figure 1). **Figure 15** shows that ejection through planetary scattering is unlikely to occur from the inner regions of the known planetary systems, which is consistent with the idea that most interstellar interlopers are ice-rich bodies formed beyond their snow-lines (see the discussion in Section 4.6). Unfortunately, given the uncertainties in the architectures and evolution of other planetary systems, it is not possible to meaningfully estimate the galactic rate of ejection to the ISM other than by measurements of the interloper population.

Whatever the mechanism, objects that are ejected from close to the host star must acquire higher velocities than those launched from more distant locations in order to overcome the gravity of the star. These higher velocities require scattering from more massive planets and, in planetary systems like our own, high-velocity ejections should be rare. Therefore, unless the progenitor system is a special case like a circumbinary system, where it is easier to eject from closer in, ejection at high velocity should be less common. A first-order corollary of this is that the galactic distribution of velocities of interstellar objects upon ejection should closely resemble the well-known kinematic distribution of stars.[3]

[3]These dispersions would be modified by subsequent dynamical heating.

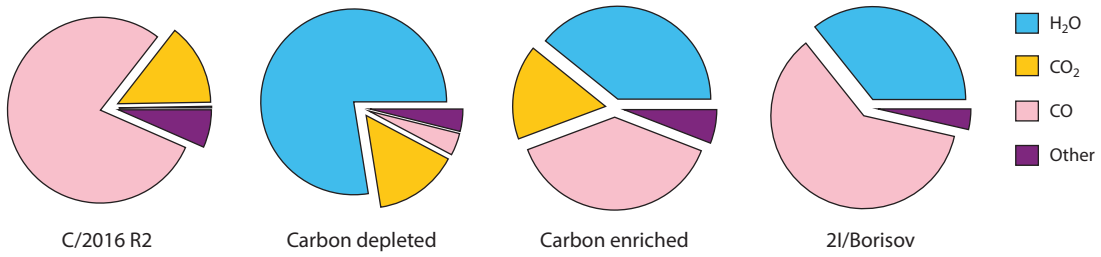


**Figure 16**

The composition of the LPC C/2016 R2, 2I/Borisov, and typical carbon-enriched and depleted Solar System comets. The carbon-depleted comet is representative of many of the Solar System comets for which production rate measurements of $CO_2$, CO, and $H_2O$ exist (see Seligman et al. 2022, their table 1). The carbon-enriched comet is W3 Christensen (Ootsubo et al. 2012). The composition for 2I/Borisov is derived from **Table 4** and references therein, and R2 is from McKay et al. (2019). The lack of $CO_2$ for 2I is only because no measurement of $CO_2$ was obtained. This is a generalized version of an analogous figure of McKay et al. (2019) and adapted from Seligman et al. (2022). Abbreviation: LPC, long-period comet.

### 4.6. 2I as a More "Normal" Comet

The $Q(CO)/Q(H_2O) \sim 1$ production rate ratio in 2I/Borisov (Bodewits et al. 2020, Cordiner et al. 2020) distinguishes this object from most Solar System comets, in which $H_2O$ is usually the dominant molecule (**Figure 16**). The average cometary ratio is $Q(CO)/Q(H_2O) \sim 4\%$, albeit with a wide range from 0.5% to 20% (Bockelée-Morvan et al. 2022). However, a few exceptionally CO-rich comets exist. For example, C/1995 O1 (Hale–Bopp) had $Q(CO)/Q(H_2O) > 12$ at $r_H = 6$ AU (Biver et al. 2002), whereas SPC/Centaur 29P/Schwassmann-Wachmann 1 had $Q(CO)/Q(H_2O) = 10 \pm 1$, also at $r_H \sim 6$ AU (Biver et al. 2002, Bockelée-Morvan et al. 2022). The outstanding example is C/2016 R2, in which $Q(CO)/Q(H_2O) = 308 \pm 35$ at $r_H \sim 2.8$ AU (McKay et al. 2019) (a limit of $Q(CO)/Q(H_2O) > 10$ was set independently by Biver et al. 2018). C/1995 O1 (Hale–Bopp) and C/2016 R2 have barycentric orbital eccentricities $e < 1$ and are from the Oort cloud, whereas 29P is a recent arrival from the Kuiper belt.

How can these large $Q(CO)/Q(H_2O)$ ratios be understood? One effect is distance; the $Q(CO)/Q(H_2O)$ in a given object should naturally grow with $r_H$ because the volatility of water ice falls faster with $r_H$ than does that of CO. This contributes to the high ratios in 29P and C/1995 O1 at 6 AU, where water is largely frozen out. However, 2I/Borisov and C/2016 R2 were observed at much more modest heliocentric distances (~2 to 2.5 AU), and the distance effect can be ignored.

A second effect is that the outgassed species might not represent the bulk composition of the nucleus. For example, highly volatile CO molecules can be mobilized at much lower temperatures than $H_2O$ molecules, providing a source zone extending more deeply into the nucleus. This effect must be transient, because CO could be depleted from the thermally heated skin of the nucleus long before the water ice is sublimated away. But the effect is difficult to model, because cometary volatiles exist within a complex, porous regolith with a large and varying temperature profile and unmeasured permeability to deep gas flow.

The most interesting interpretation of these observations is that supervolatile-enriched objects like 2I/Borisov and C/2016 R2 were accreted at very large stellocentric distances compared to most of the comets remaining in the short- and long-period populations. Comets formed at large distances beyond the CO snow-line would be the least strongly bound to their parent star and perhaps the most likely to be lost to interstellar space. If so, we should expect to find higher average $Q(CO)/Q(H_2O)$ in interstellar interlopers than in the bound comets.

**4.6.1. Evidence from protoplanetary disks.** The study of interstellar interlopers is closely related to the field of protostellar disk evolution. Recent observations that resolve protostellar disk substructure are beginning to revolutionize our understanding of the earliest stages of planet formation (Manara et al. 2022, Miotello et al. 2022). Observations of face-on disks have revealed the ubiquity of remarkable structures including gaps, spirals, and rings (Andrews et al. 2018, Long et al. 2018, Andrews 2020, Francis & van der Marel 2020, Öberg et al. 2021, Benisty et al. 2022). Protostellar gas disks are typically a factor of two larger than disks of millimeter-sized dust grains, which is possibly a result of radial migration of the dust under gas drag (Ansdell et al. 2018).

Disk observations from near the projected mid-plane allow for the measurement of the vertical scale heights of both gas and dust. Gas is vertically supported by a pressure gradient while, in the absence of substantial turbulence, dust settles toward the mid-plane under the action of stellar gravity. As a result, the dust mass density in the mid-plane grows toward a critical value. In the modern view, a streaming instability is triggered if the dust-to-gas ratio of ∼1 is reached (Youdin & Goodman 2005) and the subsequent agglomeration of macroscopic bodies is rapid. Although volatile molecules can be trapped in water either as clathrates or in the amorphous form, bulk ice can only freeze past the snow line. Therefore, we are especially interested in measurements of disk structure, including the disk scale heights in gas and dust, at the largest distances from the parent star.

Villenave et al. (2022) presented Atacama Large Millimeter/submillimeter Array (ALMA) images of the protoplanetary disk Oph163131 (J163131.2-242627), whose disk is inclined to the line of sight by only $i \sim 6$ deg. The scale height in millimeter-sized dust is ∼0.5 AU at 100 AU from this Sun-like star (the mass is $1.2 \pm 0.2\ M_\odot$), compared with a scale height in $^{12}$CO gas of ∼10 AU at the same distance (**Figure 17**). Enhanced mid-plane densities may allow macroscopic bodies to grow rapidly in this disk, even at 50 AU to 100 AU from the star. Oph163131 thus constitutes a possible analog for the formation site of CO-rich 2I/Borisov (Bodewits et al. 2020, Cordiner et al. 2020). Other works also find a dust scale height of ∼1 AU at 100 AU from the central star (Pinte et al. 2016, Villenave et al. 2020, Doi & Kataoka 2021).

Given the greater abundance of $H_2O$ ice relative to CO in molecular clouds and protoplanetary disk gas, some mechanism of concentration is needed to account for comets in which $CO/H_2O \gtrsim 1$. Radial transport of solids under the action of viscous forces may play a role. New models

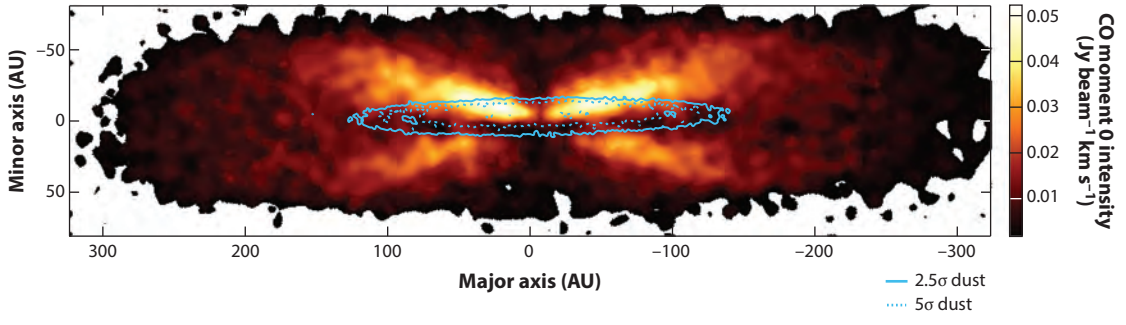


**Figure 17**

ALMA continuum and CO observations of the edge on protoplanetary disk SSTC2D J163131.2-242627 (Oph163131, $i \sim 84$ deg). The color scale shows the $^{12}$CO intensity map from ALMA observations. The blue solid and dashed lines show 2.5 and 5$\sigma$ contours of the dust continuum from ALMA. The gas is significantly more extended in the vertical direction than the dust (with scale heights different by more than an order of magnitude), implying conditions amenable for supervolatile-enriched planetesimal formation at large stellocentric distances. Data taken and figure adapted with permission from Villenave et al. (2022). Abbreviation: ALMA, Atacama Large Millimeter/submillimeter Array.

including both the migration of solids and the diffusion and freezing of CO gas in a protoplanetary disk show the formation of an extensive region in which grains grow with $CO/H_2O > 1$ (Krijt et al. 2020, Price et al. 2021, Estrada & Cuzzi 2022). These models are highly idealized, involving many assumptions and poorly characterized physical processes. However, the growth of a CO-enriched region, spanning from about 10 AU to 100 AU after $10^6$ years of disk evolution, appears to be a consistent result. Such regions could be the source of CO-enhanced comets and interstellar objects.

Perversely, the above models predict CO enrichment over such a large fraction of the protoplanetary disk that one wonders why CO-enriched comets are observationally rare. A possible answer is given by Lisse et al. (2022), who argued that the final supervolatile abundances of comets should also depend on their disk residence time prior to ejection from the parent star. For example, Steckloff et al. (2021) argued that the solar radiation received by Arrokoth and other cold-classical KBOs, when integrated over >10–100-million-year timescales, would be sufficient to deplete all subsurface supervolatiles. Comets ejected to interstellar space soon after their growth can preserve a high CO fraction, whereas those lingering longer would lose the bulk of their supervolatiles by sublimation. In this view, the low $Q(CO)/Q(H_2O)$ in most measured comets reflects a long interval between the growth of the nucleus and the formation of the Oort cloud. CO-enriched objects like C/2016 R2 and 2I/Borisov would then have preserved their CO by virtue of unusually early ejection from the parent disks. The apparent rarity of CO-enriched comets may simply reflect the time profile of cometary ejection. Furthermore, LPCs and SPCs do not exhibit strong compositional differences, perhaps reflecting formation within the giant planet region between the CO and $H_2O$ snow lines (A'Hearn et al. 2012, Ootsubo et al. 2012, Harrington Pinto et al. 2022, Seligman et al. 2022).

Unfortunately, even in the Solar System, the details of cometary accretion are subjects of uncertainty and contention (Davidsson 2021) and the timing of Oort cloud formation is essentially unknown, making these ideas difficult to test. Still, it is evident that future measurement of the distribution of compositions of interstellar interlopers will provide insights into both the timing and the structure and evolution of the disks from which they are likely ejected.

## 5. STATISTICS AND ORIGINS

### 5.1. Galactic Population

Prior to the discovery of 1I and 2I, only upper limits to the galactic number density of interstellar bodies could be estimated. These estimates are scattered over a wide range, depending on assumptions made about the observational parameters of different surveys and about the nature and distribution of the sources of interlopers. The most sophisticated estimates were not necessarily the most accurate.

The detection of 'Oumuamua in the relatively well-characterized Pan-STARRS (Panoramic Survey Telescope & Rapid Response System) sky survey allows for more confident estimates of the galactic number density of similar bodies. The value is now estimated to be between $n_0 \sim 0.1$ AU$^{-3}$ (Jewitt et al. 2017, Trilling et al. 2017) to 0.2 AU$^{-3}$ (Do et al. 2018). As 5 years have elapsed since the discovery of 'Oumuamua without another detection of a similar object, we adopt the lower estimate, $n_0 \sim 0.1$ AU$^{-3}$. This corresponds to $\sim 10^4$ similar objects closer to the Sun than Neptune (i.e., distance of $\leq$30 AU) at any instant. With a Solar System crossing time $\sim$10 years, the flux of interlopers into the planetary region is an incredible $\sim 10^3$ year$^{-1}$ (3 day$^{-1}$).

Considering the galaxy as a disk of radius 10 kpc and thickness 1 kpc, this density implies a population of $\sim 10^{26}$ objects of 100-m scale, with a combined mass of $\sim 6 \times 10^{35}$ kg ($10^{11}$ $M_\oplus$, or about 1 $M_\oplus$ per star). This is comparable with the canonical $\sim$1 $M_\oplus$ estimated mass of the Oort cloud but refers to objects 10 times smaller than the nominal LPC nucleus. The total interloper

mass must be larger but very uncertain because our estimate is based on a single object and because interstellar objects presumably occupy a size distribution in which the mass is dominated by objects larger than 'Oumuamua. Given these uncertainties, it is not yet clear if the inferred interloper population contradicts the hypothesis that these objects are ejected comets.

Conversely, 2I/Borisov was discovered as part of a near-Sun survey whose depth and areal coverage have not been published, making it impossible to estimate a useful number density. Furthermore, 2I was discovered because of its bright coma, the uncertain optical properties of which would undercut any attempt to derive a meaningful object number density. For these reasons, it is not possible to use the detection of the second interloper to strengthen the density estimate obtained from 'Oumuamua.

## 5.2. Dynamics

Gravitational interactions with GMCs and other substructures in the disk of the galaxy cause a progressive excitation of the velocities of passing stars and tracer particles. This process of disk heating should similarly excite the motions of interstellar bodies, providing a method to estimate the length of time they have spent in the interstellar environment. In fact, because interstellar objects outnumber stars by many orders of magnitude, the population is in principle a much better realization of the fine-grain assumption in the collisionless Boltzmann equation. **Figure 18** shows an empirical stellar age versus velocity dispersion relation together with the excess velocities relative to the local standard of rest of both interlopers (Holmberg et al. 2009). 'Oumuamua's low velocity (26 km $s^{-1}$, compared to 15 $\pm$ 2 km $s^{-1}$ for the velocity of the Sun relative to the local standard of rest Robin et al. 2017) implies an age $\tau_S \sim 100$ Myr, originally noted by Gaidos et al. (2017), Mamajek (2017), and Hallatt & Wiegert (2020). The larger velocity of 2I/Borisov (32 km $s^{-1}$), indicates greater disk heating and therefore a greater age since ejection, probably $\tau_S \sim 10^9$ years (Hallatt & Wiegert 2020). Notable limitations are (*a*) these estimates are statistical in nature and also subject to surprisingly large systematic uncertainties in the velocity of the Sun

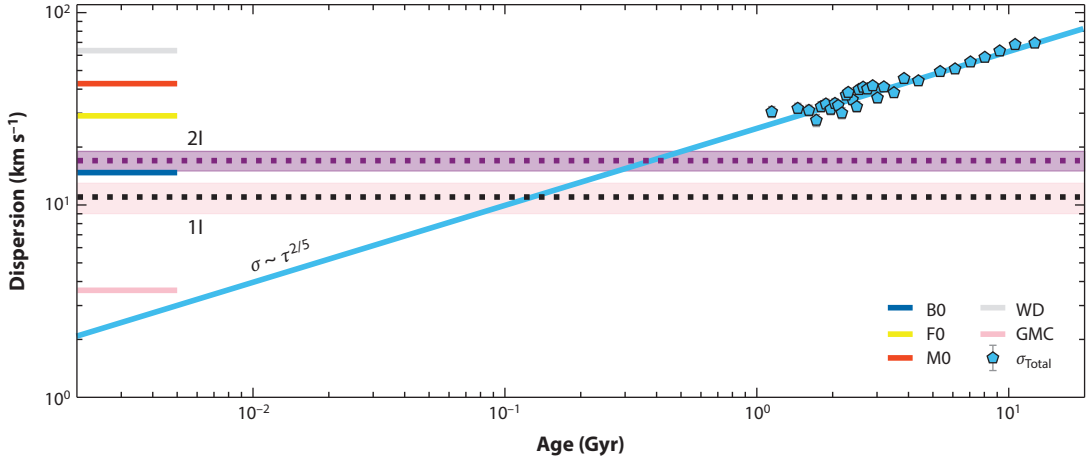


**Figure 18**

Age kinematics of stars and interstellar interlopers. Blue pentagonal points show average measured stellar velocity dispersions (data from Holmberg et al. 2009, their figure 7), with a best fit $\sigma \sim \tau^{2/5}$ as a blue solid line. The black and purple dotted lines indicate the velocity for 1I/'Oumuamua and 2I/Borisov (with only statistical uncertainties shaded). Median measured dispersions of B, F, and M stars; WDs (data from Binney & Merrifield 1998); and GMCs (data from Miville-Deschênes et al. 2017) are indicated with solid lines on the left-hand axis. Abbreviations: GMC, giant molecular cloud; WD, white dwarf.

(Schönrich et al. 2012 versus Robin et al. 2017) and (*b*) they depend on a considerable extrapolation of the stellar data (**Figure 18**). The strongest conclusion is that 1I/'Oumuamua is likely to have spent less time in interstellar space than 2I/Borisov.

If its age is only ∼100 Myr, 'Oumuamua could not have traveled far from its origin. Gaidos et al. (2017) identified a match with the 45 ± 10 Myr old Carina and Columba moving groups (comoving but unbound aggregates of recently formed stars; Bell et al. 2015). They suggested that 'Oumuamua formed in a protostellar disk around a star there and was ejected with low peculiar velocity to explain the kinematics. Independent dynamical integrations of the galactic trajectory confirm that 'Oumuamua was likely associated with the local Orion Arm, consistent with the Carina or Columba stellar associations (Hallatt & Wiegert 2020). Hsieh et al. (2021) argued that this was evidence that the object was produced in a GMC core, instead of a protostellar disk—because these cloud products would have significantly lower velocity dispersions due to the transient nature of star-forming regions in the galaxy. Although linkage to a general region of the galaxy is possible, attempts to identify the particular star from which 'Oumuamua was ejected are futile, given the many observational and dynamical uncertainties (e.g., the time and distance dependence of the nongravitational acceleration) (Zhang 2018). There is even less hope of identifying a home system for the much older 2I/Borisov (Hallatt & Wiegert 2020).

One consequence of a local origin for 'Oumuamua is that the inferred density of similar objects, $n_0 \sim 0.1$ AU$^{-3}$, may not apply uniformly to the whole galaxy. Moro-Martín (2018) argued that 'Oumuamua was ejected from the planetesimal disk of a young nearby star and that this ejection was highly anisotropic. Hsieh et al. (2021) traced the motions of test particles ejected from stars in the Carina and Columba stellar associations and found them to be statistically consistent with the orbit of 'Oumuamua. They inferred ejection speeds of ∼1 km s$^{-1}$.

## 5.3. Effects of the Interstellar Environment on the Interlopers

Direct interactions between stars and interlopers are extraordinarily rare. The timescale for a single object to pass within a distance, $d$, of a star is just $t \sim (\pi N_\star \Delta V d^2)^{-1}$, where $N_\star \sim 0.1$ pc$^{-3}$ is the number density of stars, and $\Delta V = 50$ km s$^{-1}$ is the nominal velocity dispersion. The paths of interlopers are affected by gravitational focusing, which increases the effective cross-section by a factor of $\sim(V/\Delta V)^2$, where $V$ is the local escape speed at the minimum distance from the star. For example, a Sun impact would have $d \sim 10^9$ m and $V/\Delta V \sim (600/50)^2 \sim 140$. Substituting, we find $t \sim 10^{17}$ years, showing that the probability for a given interloper to collide with a star is negligible. Even interactions as close as those of 'Oumuamua (minimum distance $d = 0.25$ AU) and 2I/Borisov ($d = 2.0$ AU) are incredibly unlikely ($t \sim 10^7$ Gyr) for a given object. As a result, the preentry thermal evolution of interstellar interlopers should be minimal. Their surface temperatures, set by equilibrium with the interstellar UV flux, will be just a few degrees above the microwave background temperature.

By contrast, the interlopers travel through and interact with the gas and dust of the ISM. Stern (1990) showed that while some mass is added by the implantation of interstellar gas into the surfaces of Oort cloud comets (which are as fully exposed to the ISM as are the interlopers), much more material is eroded by impact with interstellar dust grains. The net effect is the loss of the upper $\Delta L \sim 0.1$ m of surface for every billion years of exposure. Compared to the size scales of 'Oumuamua and 2I/Borisov, the lost material is mass-wise unimportant. Only decimeter-scale and smaller interstellar debris should be substantially depleted by impact erosion on billion-year timescales.

Interstellar space is also pervaded by cosmic rays, with energies that are orders of magnitude greater than the few electronvolt binding energies of common molecular bonds. Cosmic rays

severely damage the molecular structure of materials with which they interact. In the open ISM, the cosmic-ray energy spectrum resembles a broken power law, having the largest fluences at the smallest energies. (The energy spectrum in the Kuiper belt is different, owing to shielding of low-energy particles by the Sun's magnetic field). The cosmic-ray penetration depths into solid matter, $d_{CR}$, depend on the particle energies, $E$. For $E \lesssim 0.1$ GeV, the penetration depths, $d_{CR} < 0.1$ m (Cooper et al. 2003, Gronoff et al. 2020), are smaller than the impact-eroded layer thickness. With $d_{CR} < \Delta L$, the degree of surface processing by low-energy particles is limited by the steady loss of surface material to impact and the continual exposure of fresh material from beneath. However, the energetic $E \gtrsim 1$ GeV protons and alpha particles have much larger penetration depths in ice, $d_{CR} \sim 1$ m to 10 m. Because $d_{CR} > \Delta L$, comets and interstellar interlopers should develop a processed surface layer or crust that is too thick to be eroded away by impact with interstellar dust.

Laboratory experiments show that the principal effect of energetic particle bombardment is to sever molecular bonds, resulting in the formation of new bonds (and radicals). Being light, hydrogen atoms easily escape, leading to a progressive buildup of macromolecular, carbon-rich solids (Henderson & Gudipati 2015). This irradiated material can have low volatility and very low albedo, which is quite different from the initial material. An unfortunate consequence of the destruction of bonds is that irradiated materials lack the characteristic vibrational spectral features on which spectroscopic chemical identifications are based (e.g., Faure et al. 2021). Probably for this reason, the reflection spectra of most comets, like those of 'Oumuamua and 2I/Borisov, tend to be linear, featureless, and difficult or impossible to compositionally diagnose. The similarity between the redder-than-sunlight colors of the interlopers and those of Solar System comets (Section 3.2) is broadly consistent with cosmic-ray processing of both but is not diagnostic of composition.

## 5.4. Capture of Interstellar Objects

Some of the Sun's Oort cloud comets might have been captured from the Oort clouds of nearby stars, aided by the very low velocity dispersion in the Sun's presumed birth cluster (Levison et al. 2010). Galactic tides, although very weak, can temporarily trap slowly passing interstellar objects on loosely bound orbits, building a swarm of such bodies estimated to number $\sim 10^7$ within ~20,000 AU (Peñarrubia 2022). Likewise, a small fraction of the interstellar objects passing through the planetary region of the Solar System can be trapped by gravitational interactions with the planets, albeit with very low and strongly encounter-velocity-dependent efficiency (Napier et al. 2021a, Dehnen & Hands 2022). The action of nongravitational acceleration could also trap smaller objects. Napier et al. (2021b) calculated that the total mass of interstellar objects trapped in the Solar System was $\sim eq 10^{-9}$ $M_\oplus$, by estimating their typical dynamical lifetimes. Most of this interstellar material in the present day Solar System was captured during the Sun's cluster phase. Under a different set of assumptions, Dehnen & Hands (2022) argued that there should be only ~8 interstellar objects captured within 5 AU at any given time.

Although the statistics of capture are forbidding, it has nevertheless been suggested that some Centaurs and Trojans with extreme orbits could be captured interstellar bodies (Namouni & Morais 2020). However, it is more likely that these objects are transient captures from distant Solar System reservoirs, such as Halley-type comets or the Oort cloud (Morbidelli et al. 2020).

In this regard, just as there is a small probability for unbound objects to become trapped into bound orbits, it is possible for comets from our own Oort cloud to be scattered onto hyperbolic orbits through interactions with passing stars and substellar objects. On rare occasions, ejected Oort cloud comets passing through the planetary region might be mistaken for interstellar interlopers arriving from afar. Higuchi & Kokubo (2020) estimated that about 0.1% of objects with

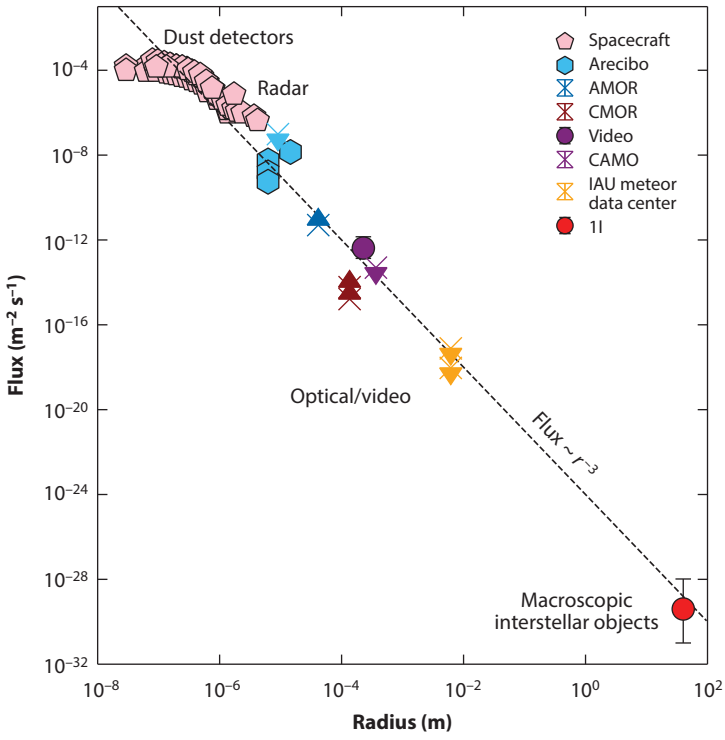


**Figure 19**

Observational constraints on the fluxes of interstellar bodies. The observations consist of (*pink pentagons*) in-situ dust detections from the *Ulysses* and *Galileo* spacecraft (Grün et al. 1993, 1997, 2000; Landgraf & Grün 1998; Landgraf et al. 2000), (*blue hexagons*) radar measurements from Arecibo (Mathews et al. 1999; Meisel et al. 2002a,b), radar lower limits with the (*dark blue X*) AMOR (Baggaley et al. 1993, Taylor et al. 1996, Baggaley 2000) and (*red X*) CMOR (Weryk & Brown 2004), (*purple triangle*) optical data from Hawkes et al. (1999) and CAMO (Musci et al. 2012), and (*orange X*) upper limits from optical images of meteoroids from the photographic database of the IAU Meteor Data Center (Hajduková 1994, Hajduková & Paulech 2002). The flux inferred from the 0.1 $AU^{-3}$ density of 1I/'Oumuamua-like objects is also shown as a red filled circle. Other than the micron-sized dust and 'Oumuamua points, a majority of the measurements should be taken as upper limits to the flux. The line is added to guide the eye and is not a fit to the data. Figure adapted with permission from Musci et al. (2012). Abbreviations: AMOR, Advanced Meteor Orbit Radar; CAMO, Canadian Automated Meteor Observatory; CMOR, Canadian Meteor Orbit Radar; IAU, International Astronomical Union.

orbits similar to 'Oumuamua, and 0.01% of those similar to the more eccentric orbit of 2I/Borisov, could originate as comets deflected from our own Oort cloud. Although these probabilities depend on poorly constrained estimates of the number density of nearby substellar and even sub-Jovian perturbers, it is clear that almost all unbound objects entering the planetary region originate from elsewhere in the galaxy.

## 5.5. Interstellar Meteors and Impactors

Existing constraints on the flux of interstellar particles near Earth across a wide range of sizes are shown in **Figure 19**. The data in **Figure 19** are broadly compatible with an $r_n^{-3}$ radius distribution, subject to a roll over at sizes of $r_n \lesssim 0.1$ μm. The latter occurs because dust particles smaller than ∼0.1 μm are largely deflected from the inner Solar System by a combination of radiation pressure

and Lorentz forces. Slightly larger particles (radius of $\gtrsim$0.4 μm) can penetrate and have been recorded from impact detectors on spacecraft, with a flux of $\sim 10^{-4}$ m$^{-2}$ s$^{-1}$ (Gruen et al. 1994; see **Figure 19**). These interstellar dust particles can be reliably identified because their velocities are accurately measured using time-of-flight detectors and found to be higher than the local Solar System escape speed.

Millimeter-sized interstellar particles should, in principle, give rise to meteors, which should also be readily identifiable by their velocities.[4] However, rather stringent measurements of speed (accurate to $\pm 1$ km s$^{-1}$) and of direction (to $\pm 1$ deg or 2 deg) are needed to distinguish some hyperbolic from bound orbits (cf. Hajduková et al. 2020). Unfortunately, measurements of sufficient accuracy are difficult given the short flight lengths (a few $\times 10$ km) and times ($\sim$1 s) of meteors in the atmosphere. As a result, there is a long history of false detections of interstellar meteors. Famously, Öpik (1934) used optical data to infer high speeds requiring a substantial fraction of terrestrial meteors to be of interstellar origin, a result that we now know to be wholly incorrect. Similarly, Peña-Asensio et al. (2022) and Siraj & Loeb (2022) claimed that a previously reported meteor was interstellar but unfortunately relied, in part, on secret (US Department of Defense) satellite data concerning the accuracy of the trajectory. The interstellar claim has been subsequently refuted (Vaubaillon 2022). Interferometric radar determinations of meteor velocities (Baggaley et al. 2007) show that most meteors are unambiguously bound and thus have a Solar System origin, with only a small high-velocity tail, again likely due to measurement errors (Musci et al. 2012).

Large interstellar objects must occasionally strike the Earth but, because of their high-impact velocities, they are less likely than asteroids to deposit meteorites onto the surface. The rate of impact of 100-m-scale interstellar bodies into Earth is $\sim 5$–$10 \times 10^{-9}$ year$^{-1}$ (Jewitt et al. 2020a), giving only 25 to 50 such events over the age of the Earth, with many of these exploding above the ground as airbursts. This estimated rate is $\sim 10^4$ times less than the rate of impact by Solar System material (mostly asteroids) of comparable size. Therefore, we are unlikely to find evidence for craters formed by interstellar projectiles or for interstellar meteorites in our collections. Even if the flux were higher, it is unclear how to distinguish a crater formed by an interstellar impact from one formed by a Solar System projectile (Cabot & Laughlin 2022).

Young planetary systems are capable of ejecting objects with an enormous range of size scales, from dust to planets (Moro-Martín 2019). The mass distribution of free-floating planets extended to include 1I/'Oumuamua is approximately represented by a differential power law with an index, $p = 0.89 \pm 0.06$ (Gould et al. 2022), corresponding to a size distribution with an index of $3.7 \pm 0.2$. The similarity between this estimate and the one in **Figure 19** is most likely coincidental. However, these two indices are compatible within the uncertainties for objects of much smaller size. Future discoveries of both free floating planets and interstellar objects should clarify the nature of this underlying distribution.

## 6. FUTURE PROSPECTS

### 6.1. Ground Based

It is possible that interstellar objects in the Solar System have been recorded but went unnoticed in existing survey data. A systematic search for such objects in archival data would be a valuable first step toward improving our population estimates, even before the advent of powerful, new sky survey telescopes. Many new interstellar interlopers are expected to be found by both the

[4]Although $e > 1$ is a necessary condition for the identification of interstellar material, it is not definitive, because planetary perturbations can generate hyperbolic trajectories, albeit with excess velocities of only $\sim$0.1 km s$^{-1}$ (Wiegert 2014, Higuchi & Kokubo 2020).

**Table 7 Predicted detection rates of interstellar objects[a]**

| Criterion | Percent | Conservative rate per year | Optimistic rate per year |
|---|---|---|---|
| Detectable by the LSST | 2.828% | ~0.9 | ~1.9 |
| Detectable, $\Delta V < 15$ km s$^{-1}$ | 0.424% | ~0.1 | ~0.3 |
| Detectable, $\Delta V < 2$ km s$^{-1}$ | 0.002% | ~0.0007 | ~0.001 |

[a]Table adapted from Hoover et al. (2022). 'Oumuamua-like absolute magnitude, H = 22.4 assumed from (Hoover et al. 2022).



planned and already operational all-sky surveys. In particular, the Rubin Observatory Legacy Survey of Space and Time (LSST) should offer a substantial increase in sensitivity to transient objects while surveying the entire night sky in the Southern Hemisphere with a close to nightly cadence (Moro-Martín et al. 2009, Cook et al. 2016, Engelhardt et al. 2017, Seligman & Laughlin 2018). Hoover et al. (2022) used an elaborate simulation to estimate not only the LSST detection rates as a function of size and absolute magnitude but also the distribution of orbital elements and trajectories of detectable interstellar objects. They predicted that the LSST will detect between 1 and 2 'Oumuamua-like interstellar objects every year (for details see **Table 7**).

The flux curve in **Figure 19** indicates that meter-sized interstellar objects, with a flux of $f \sim 10^{-24}$ m$^{-2}$ s$^{-1}$, should strike Earth's atmosphere on a $t \sim (4\pi R_\oplus^2 f)^{-1} \sim 10^2$-year timescale. It is therefore not surprising that convincing examples of hyperbolic bolides have yet to be reported. However, the cumulative fluxes of 1-cm- and 10-cm-scale interstellar meteors should be higher by 4 and 2 orders of magnitude, respectively, corresponding to timescales from a few days to a year. These timescales approach the duration of long-term meteor surveys, such that we can reasonably hope for convincing detections of small-scale interstellar meteors in the next few years, provided that adequate velocity resolution can be attained. Firm detections of material in the centimeter- to decimeter-size range would help bridge the gap between the spacecraft-detected micron-sized interstellar dust particles and the macroscopic objects discussed here.

## 6.2. Space Based

In space, the forthcoming *Near-Earth Object Surveyor* (NEO Surveyor) (consisting of a 50-cm-diameter telescope located interior to Earth's orbit at L1; Mainzer et al. 2015) is expected to provide thermal infrared (10 μm) detections and orbits of small bodies out to the orbit of Jupiter, with a sensitivity to near-Earth objects rivaling that of the LSST. Located interior to Earth's orbit, it will also provide greater coverage of the sky at small elongation (Sun-telescope-object) angles than is possible with a large telescope from the ground. This allows for the detection of objects at heliocentric distances $r_H < 1$ AU. Combined with optical data, NEO Surveyor thermal flux density measurements will break the degeneracy between the sizes and albedos that afflicts optical data alone. Thermal data from *James Webb Space Telescope* can also fulfill this role, albeit with much more restricted telescope pointing constraints.

Recently, the European Space Agency selected the *Comet Interceptor* (Jones 2019) to launch in 2029. The *Interceptor* has a low $\Delta V \sim 1$ km s$^{-1}$ budget and can only reach objects whose orbits bring them fortuitously close to its loitering location at L2 within the 3-year duration of its mission (Sánchez et al. 2021). With these mission parameters, the likelihood that *Interceptor* will find an accessible interstellar target is negligible (cf. **Table 7**; Hoover et al. 2022). More optimistically, an impactor mission to 'Oumuamua, sent from the Earth, would have been achievable with a modest impulse ($\Delta V \sim 4$ km s$^{-1}$) given sufficient forewarning of the approach (Seligman & Laughlin 2018). Hoover et al. (2022) estimated that 10% to 30% of the interstellar interlopers

to be detected by the LSST will be reachable by a mission with $\Delta V < 15$ km s$^{-1}$ (Hoover et al. 2022). Optimistically, a handful of rendezvous-suitable targets will be detected each decade.

## SUMMARY POINTS

1. The two currently known interstellar interlopers are subkilometer bodies with surprisingly different properties. 1I/'Oumuamua appears asteroid-like while exhibiting strong nongravitational acceleration of unknown origin. 2I/Borisov is overall more comet-like in showing nongravitational acceleration consistent with its outgassing rate but is richer in CO than most Solar System comets.
2. It is not clear whether these differences reflect two entirely different populations or different evolutionary stages of the same type of object.
3. The number density of 'Oumuamua-like (100 m scale) bodies is $\sim$0.1 AU$^{-3}$, whereas the implied galactic population is $\sim 10^{25}$ to $10^{26}$.
4. The relative velocities at infinity suggest that 1I/'Oumuamua has spent less time in interstellar space than 2I/Borisov.
5. Interlopers formed by accretion in protoplanetary disks are ejected to interstellar space by strong gravitational scattering from planets. 'Oumuamua is tentatively associated with the Carina or Columbia stellar associations. The origin of 2I/Borisov is unknown.

## FUTURE ISSUES

1. Current interloper population estimates are extremely uncertain but of great importance in relation to the likely protoplanetary disk origins of these bodies and their galactic total mass.
2. Physical measurements of interstellar interlopers are needed to understand the reason for the divergent appearances of the first two examples and to better relate these bodies to Solar System comets.
3. Planned deep, all-sky surveys (in particular, by NASA's *Near-Earth Object Surveyor* and by the Legacy Survey of Space and Time are expected to reveal new interstellar interlopers each year.
4. Spacecraft intercepts of interlopers will be possible but difficult, given the high average encounter velocities and limited forewarning of arrival.

## DISCLOSURE STATEMENT

The authors are not aware of any affiliations, memberships, funding, or financial holdings that might be perceived as affecting the objectivity of this review.

## ACKNOWLEDGMENTS

We thank Marion Villenave, Karen Meech, and Olivier Hainaut for providing us with data and Amaya Moro-Martin, Robert Jedicke, Garret Levine, Davide Farnocchia, Yoonyoung Kim, Marco Micheli, Greg Laughlin, Aster Taylor, Jane Luu, Pedro Lacerda, Amy Mainzer, Adina

Feinstein, Andrew Youdin, Jing Li, Benjamin Donitz, Alan Stern, Maria Hajduková, Fred Adams, Juliette Becker, and Sophie Deam for useful conversations and suggestions. D.Z.S. acknowledges financial support from the National Science Foundation grant no. AST-17152, NASA grant no. 80NSSC19K0444, and NASA Contract NNX17AL71A from the NASA Goddard Spaceflight Center.

## LITERATURE CITED

A'Hearn MF, Feaga LM, Keller HU, et al. 2012. *Ap. J.* 758:29
Andrews SM. 2020. *Annu. Rev. Astron. Astrophys.* 58:483–528
Andrews SM, Huang J, Pérez LM, et al. 2018. *Ap. J. Lett.* 869(2):L41
Ansdell M, Williams JP, Trapman L, et al. 2018. *Ap. J.* 859:21
Aravind K, Ganesh S, Venkataramani K, et al. 2021. *MNRAS* 502(3):3491–99
Baggaley WJ. 2000. *J. Geophys. Res.* 105(A5):10353–62
Baggaley WJ, Marsh SH, Close S. 2007. In *Workshop on Dust in Planetary Systems*, *ESA SP-643*, ed. H Krueger, A Graps, pp. 27–32. Noordwijk, Neth.: ESA Publ. Div. ESTEC
Baggaley WJ, Porubcan V, eds. 1999. *Meteoroids 1998: Proc. Intl. Conf. Held Tatranska Lomnica*, *Slovakia*, *August 17–21*, *1998*. Bratislavia, Slovak.: Astron. Inst., Slovak Acad. Sci.
Baggaley WJ, Taylor AD, Steel DI. 1993. In *Meteoroids and their Parent Bodies*, *Proc. Intl. Astron. Symp.*, Smolenice, Slovakia, July 6–12, 1992, Bratislava: Astron. Inst., Slovak Acad. Sci.
Bannister MT, Opitom C, Fitzsimmons A, et al. 2020. arXiv:2001.11605
Bannister MT, Schwamb ME, Fraser WC, et al. 2017. *Ap. J. Lett.* 851(2):L38
Bell CPM, Mamajek EE, Naylor T. 2015. *MNRAS* 454:593–614
Belton MJS, Hainaut OR, Meech KJ, et al. 2018. *Ap. J. Lett.* 856:L21
Benisty M, Dominik C, Follette K, et al. 2022. arXiv:2203.09991
Bialy S, Loeb A. 2018. *Ap. J. Lett.* 868:L1
Binney J, Merrifield M. 1998. *Galactic Astronomy*. Princeton, NJ: Princeton Univ. Press
Biver N, Bockelée-Morvan D, Colom P, et al. 2002. *Earth Moon Planets* 90:5–14
Biver N, Bockelée-Morvan D, Hofstadter M, et al. 2019. *Astron. Astrophys.* 630:A19
Biver N, Bockelée-Morvan D, Paubert G, et al. 2018. *Astron. Astrophys.* 619:A127
Bockelée-Morvan D, Biver N. 2017. *Philos. Trans. R. Soc. A* 375(2097):20160252
Bockelée-Morvan D, Biver N, Schambeau CA, et al. 2022. *Astron. Astrophys.* 664:A95
Bodewits D, Noonan JW, Feldman PD, et al. 2020. *Nat. Astron.* 4:867–71
Bolin BT, Lisse CM, Kasliwal MM, et al. 2020. *Astron. J.* 160:26
Bolin BT, Weaver HA, Fernandez YR, et al. 2018. *Ap. J. Lett.* 852:L2
Brasser R, Higuchi A, Kaib N. 2010. *Astron. Astrophys.* 516:A72
Brasser R, Morbidelli A. 2013. *Icarus* 225:40–49
Cabot SHC, Laughlin G. 2022. *Planet. Sci. J.* 3(7):172
Childs AC, Martin RG. 2022. *Ap. J. Lett.* 935(2):L31
Combi MR, Mäkinen T, Bertaux JL, et al. 2020. *Planet. Sci. J.* 1(3):72
Cook NV, Ragozzine D, Granvik M, Stephens DC. 2016. *Ap. J.* 825:51
Cooper JF, Christian ER, Richardson JD, Wang C. 2003. *Earth Moon Planets* 92:261–77
Cordiner MA, Milam SN, Biver N, et al. 2020. *Nat. Astron.* 4:861–66
Cremonese G, Fulle M, Cambianica P, et al. 2020. *Ap. J. Lett.* 893:L12
Ćuk M. 2018. *Ap. J. Lett.* 852:L15
Davidsson BJR. 2021. *MNRAS* 505(4):5654–85
Dehnen W, Hands TO. 2022. *MNRAS* 512(3):4062–77
Desch SJ, Jackson AP. 2021. *J. Geophys. Res.: Planets* 126(5):e2020JE006807
Do A, Tucker MA, Tonry J. 2018. *Ap. J. Lett.* 855:L10
Doi K, Kataoka A. 2021. *Ap. J.* 912(2):164
Dones L, Brasser R, Kaib N, Rickman H. 2015. *Space Sci. Rev.* 197(1–4):191–269
Drahus M, Guzik P, Udalski A, et al. 2020. *Astron. Telegr.* 13549:1

Drahus M, Guzik P, Waniak W, et al. 2018. *Nat. Astron.* 2:407–12
Drahus M, Jewitt D, Guilbert-Lepoutre A, et al. 2011. *Ap. J. Lett.* 734:L4
Eisner N, Knight MM, Schleicher DG. 2017. *Astron. J.* 154(5):196
Engelhardt T, Jedicke R, Vereš P, et al. 2017. *Astron. J.* 153(3):133
Enriquez JE, Siemion A, Lazio TJW, et al. 2018. *Res. Notes Am. Astron. Soc.* 2:9
Estrada PR, Cuzzi JN. 2022. *Ap. J.* 936:40
Farnham TL, Knight MM, Schleicher DG, et al. 2021. *Planet. Sci. J.* 2:7
Faure M, Quirico E, Faure A, et al. 2021. *Icarus* 364:114462
Fernández YR, Kelley MS, Lamy PL, et al. 2013. *Icarus* 226:1138–70
Fitzsimmons A, Hainaut O, Meech KJ, et al. 2019. *Ap. J. Lett.* 885:L9
Fitzsimmons A, Snodgrass C, Rozitis B, et al. 2018. *Nat. Astron.* 2:133–37
Flekkøy EG, Luu J, Toussaint R. 2019. *Ap. J. Lett.* 885(2):L41
Francis L, van der Marel N. 2020. *Ap. J.* 892(2):111
Francis PJ. 2005. *Ap. J.* 635(2):1348–61
Fraser WC, Pravec P, Fitzsimmons A, et al. 2018. *Nat. Astron.* 2:383–86
Fulle M, Della Corte V, Rotundi A, et al. 2015. *Ap. J. Lett.* 802:L12
Gaidos E, Williams J, Kraus A. 2017. *Res. Notes Am. Astron. Soc.* 1:13
Garcia AJL, Gonzalez JF. 2020. *MNRAS* 493(2):1788–800
Gicquel A, Bockelée-Morvan D, Zakharov VV, et al. 2012. *Astron. Astrophys.* 542:A119
Gould A, Jung YK, Hwang KH, et al. 2022. *J. Korean Astron. Soc.* 55:173–94
Gronoff G, Maggiolo R, Cessateur G, et al. 2020. *Ap. J.* 890:89
Groussin O, Attree N, Brouet Y, et al. 2019. *Space Sci. Rev.* 215(4):29
Gruen E, Gustafson B, Mann I, et al. 1994. *Astron. Astrophys.* 286:915–24
Grün E, Landgraf M, Horányi M, et al. 2000. *J. Geophys. Res.* 105(A5):10403–10
Grün E, Staubach P, Baguhl M, et al. 1997. *Icarus* 129(2):270–88
Grün E, Zook HA, Baguhl M, et al. 1993. *Nature* 362(6419):428–30
Guzik P, Drahus M, Rusek K, et al. 2020. *Nat. Astron.* 4:53–57
Hahn JM, Malhotra R. 1999. *Astron. J.* 117(6):3041–53
Hainaut OR, Boehnhardt H, Protopapa S. 2012. *Astron. Astrophys.* 546:A115
Hajduková M Jr. 1994. *Astron. Astrophys.* 288:330–34
Hajduková M Jr., Paulech T. 2002. In *Proc. of Asteroids, Comets, and Meteors: ACM 2002, ESA SP-500*, ed. B Warmbein, pp. 173–76. Noordwijk, Neth.: ESA Publ. Div.
Hajduková M, Sterken V, Wiegert P, Kornoš L. 2020. *Planet. Space Sci.* 192:105060
Hallatt T, Wiegert P. 2020. *Astron. J.* 159(4):147
Hansen B, Zuckerman B. 2017. *Res. Notes Am. Astron. Soc.* 1:55
Harp GR, Richards J, Jenniskens P, Shostak S, Tarter JC. 2019. *Acta Astronaut.* 155:51–54
Harrington Pinto O, Womack M, Fernandez YR, Bauer J. 2022. *Planet. Sci. J.* 3(11):247
Hawkes RL, Close T, Woodworth S. 1999. In Baggaley & Porubcan 1999, pp. 257–64
Heinze A. 2021. *Bull. Am. Astron. Soc.* 53(7):2021n7i505p01
Henderson BL, Gudipati MS. 2015. *Ap. J.* 800:66
Higuchi A, Kokubo E. 2015. *Astron. J.* 150:26
Higuchi A, Kokubo E. 2020. *MNRAS* 492:268–75
Hoang T, Loeb A. 2020. *Ap. J. Lett.* 899(2):L23
Holmberg J, Nordström B, Andersen J. 2009. *Astron. Astrophys.* 501(3):941–47
Hoover DJ, Seligman DZ, Payne MJ. 2022. *Planet. Sci. J.* 3(3):71
Hsieh CH, Laughlin G, Arce HG. 2021. *Ap. J.* 917:20
Hui MT, Ye QZ, Föhring D, Hung D, Tholen DJ. 2020. *Astron. J.* 160(2):92
Ishiguro M, Sarugaku Y, Ueno M, et al. 2007. *Icarus* 189:169–83
Jackson AP, Desch SJ. 2021. *J. Geophys. Res.: Planets* 126(5):e2020JE006706
Jackson AP, Tamayo D, Hammond N, Ali-Dib M, Rein H. 2018. *MNRAS* 478:L49–53
Jewitt D. 2021. *Astron. J.* 161(6):261
Jewitt D. 2022. *Astron. J.* 164(4):158

Jewitt D, Hsieh HH. 2022. arXiv:2203.01397
Jewitt D, Hui MT, Kim Y, et al. 2020a. *Ap. J. Lett.* 888(2):L23
Jewitt D, Kim Y, Mutchler M, et al. 2020b. *Ap. J. Lett.* 896(2):L39
Jewitt D, Luu J. 2019. *Ap. J. Lett.* 886(2):L29
Jewitt D, Luu J, Rajagopal J, et al. 2017. *Ap. J. Lett.* 850:L36
Jewitt D, Sheppard S, Fernández Y. 2003. *Astron. J.* 125(6):3366–77
Jewitt DC. 2002. *Astron. J.* 123(2):1039–49
Jones G. 2019. *Comet Interceptor: A Mission to a Dynamically New Solar System Object*. Comet Interceptor Consortium Phase-2 Proposal. **http://www.cometinterceptor.space/uploads/1/2/3/7/123778284/cometnterceptorxecutiveummary.pdf**
Kaasalainen M, Torppa J, Muinonen K. 2001. *Icarus* 153:37–51
Kaib NA, Quinn T. 2009. *Science* 325(5945):1234–36
Kareta T, Andrews J, Noonan JW, et al. 2020. *Ap. J. Lett.* 889(2):L38
Kataoka A, Tanaka H, Okuzumi S, Wada K. 2013. *Astron. Astrophys.* 554:A4
Katz JI. 2018. *MNRAS* 478:L95–98
Kim Y, Jewitt D, Mutchler M, et al. 2020. *Ap. J. Lett.* 895(2):L34
Knight MM, Protopapa S, Kelley MSP, et al. 2017. *Ap. J. Lett.* 851(2):L31
Kokotanekova R, Snodgrass C, Lacerda P, et al. 2018. *MNRAS* 479(4):4665–80
Krijt S, Bosman AD, Zhang K, et al. 2020. *Ap. J.* 899(2):134
Lacerda P, Jewitt DC. 2007. *Astron. J.* 133(4):1393
Landgraf M, Baggaley WJ, Grün E, Krüger H, Linkert G. 2000. *J. Geophys. Res.* 105(A5):10343–52
Landgraf M, Grün E. 1998. In *IAU Colloq. 166: The Local Bubble and Beyond Lyman-Spitzer-Colloquium*, *Lect. Notes Phys.* Vol. 506, ed. D Breitschwerdt, MJ Freyberg, J Truemper, pp. 381–84. Berlin/Heidelberg: Springer
Laughlin G, Batygin K. 2017. *Res. Notes Am. Astron. Soc.* 1:43
Levine WG, Cabot SHC, Seligman D, Laughlin G. 2021. *Ap. J.* 922:39
Levine WG, Laughlin G. 2021. *Ap. J.* 912:3
Levison HF, Duncan MJ, Brasser R, Kaufmann DE. 2010. *Science* 329(5988):187–90
Lin HW, Lee CH, Gerdes DW, et al. 2020. *Ap. J. Lett.* 889(2):L30
Lisse CM, Gladstone GR, Young LA, et al. 2022. *Planet. Sci. J.* 3(5):112
Long F, Pinilla P, Herczeg GJ, et al. 2018. *Ap. J.* 869:17
Lu XP, Jewitt D. 2019. *Astron. J.* 158(6):220
Luu JX, Flekkøy EG, Toussaint R. 2020. *Ap. J. Lett.* 900(2):L22
Mainzer A, Grav T, Bauer J, et al. 2015. *Astron. J.* 149(5):172
Mamajek E. 2017. *Res. Notes Am. Astron. Soc.* 1:21
Manara CF, Ansdell M, Rosotti GP, et al. 2023. In *Protostars and Planets VII*, ed. S-I Inutsuka, Y Aikawa, T Muto, K Tomida, M Tamura. In press. Tucson: Univ. Ariz. Press. arXiv:2203.09930
Mannel T, Bentley MS, Schmied R, et al. 2016. *MNRAS* 462:S304–11
Maquet L, Colas F, Jorda L, Crovisier J. 2012. *Astron. Astrophys.* 548:A81
Marsden BG, Sekanina Z, Yeomans DK. 1973. *Astron. J.* 78:211
Mashchenko S. 2019. *MNRAS* 489(3):3003–21–25
Mathews JD, Meisel DD, Janches D, Getman VS, Zhou QH. 1999. In Baggaley & Porubcan 1999, pp. 79–82
Mazzotta Epifani E, Dotto E, Perna D, et al. 2021. *Planet. Space Sci.* 208:105341
McKay AJ, Cochran AL, Dello Russo N, DiSanti MA. 2020. *Ap. J. Lett.* 889:L10
McKay AJ, DiSanti MA, Kelley MSP, et al. 2019. *Astron. J.* 158(3):128
McNeill A, Trilling DE, Mommert M. 2018. *Ap. J. Lett.* 857:L1
Meakin P, Donn B. 1988. *Ap. J. Lett.* 329:L39–41
Mecklenburg M, Schuchardt A, Mishra YK, et al. 2012. *Adv. Mater.* 24(26):3486–90
Meech KJ, Weryk R, Micheli M, et al. 2017. *Nature* 552:378–81
Meisel DD, Janches D, Mathews JD. 2002a. *Ap. J.* 567:323–41
Meisel DD, Janches D, Mathews JD. 2002b. *Ap. J.* 579(2):895–904
Micheli M, Farnocchia D, Meech KJ, et al. 2018. *Nature* 559:223–26

Miotello A, Kamp I, Birnstiel T, Cleeves LI, Kataoka A. 2023. In *Protostars and Planets VII*, ed. S-I Inutsuka, Y Aikawa, T Muto, K Tomida, M Tamura. In press. Tucson: Univ. Ariz. Press. arXiv:2203.09818
Miville-Deschênes MA, Murray N, Lee EJ. 2017. *Ap. J.* 834:57
Morbidelli A, Batygin K, Brasser R, Raymond SN. 2020. *MNRAS* 497:L46–49
Moro-Martín A. 2018. *Ap. J.* 866(2):131
Moro-Martín A. 2019. *Ap. J. Lett.* 872(2):L32
Moro-Martín A. 2019. *Astron. J.* 157(2):86
Moro-Martín A, Turner EL, Loeb A. 2009. *Ap. J.* 704:733–42
Musci R, Weryk RJ, Brown P, Campbell-Brown MD, Wiegert PA. 2012. *Ap. J.* 745(2):161
Namouni F, Morais MHM. 2020. *MNRAS* 494(2):2191–99
Napier KJ, Adams FC, Batygin K. 2021a. *Planet. Sci. J.* 2(2):53
Napier KJ, Adams FC, Batygin K. 2021b. *Planet. Sci. J.* 2(6):217
Nesvorný D. 2018. *Annu. Rev. Astron. Astrophys.* 56:137–74
Öberg KI, Guzmán VV, Walsh C, et al. 2021. *Ap. J. Suppl.* 257:1
Oort JH. 1950. *Bull. Astron. Inst. Neth.* 11:91–110
Ootsubo T, Kawakita H, Hamada S, et al. 2012. *Ap. J.* 752:15
Öpik E. 1934. *Harvard Coll. Obs. Circ.* 389:1–9
Opitom C, Fitzsimmons A, Jehin E, et al. 2019. *Astron. Astrophys.* 631:L8
Park RS, Pisano DJ, Lazio TJW, Chodas PW, Naidu SP. 2018. *Astron. J.* 155:185
Parker AH, Kavelaars JJ. 2010. *Ap. J. Lett.* 722(2):L204–8
Peña-Asensio E, Trigo-Rodríguez JM, Rimola A. 2022. *Astron. J.* 164(3):76
Peñarrubia J. 2022. *MNRAS* 519(2):1955–80
Pfalzner S, Aizpuru Vargas LL, Bhandare A, Veras D. 2021. *Astron. Astrophys.* 651:A38
Pinte C, Dent WRF, Ménard F, et al. 2016. *Ap. J.* 816:25
Price EM, Cleeves LI, Bodewits D, Öberg KI. 2021. *Ap. J.* 913:9
Rafikov RR. 2018a. *Ap. J.* 861:35
Rafikov RR. 2018b. *Ap. J. Lett.* 867:L17
Raymond SN, Armitage PJ, Veras D. 2018. *Ap. J. Lett.* 856:L7
Raymond SN, Kaib NA, Armitage PJ, Fortney JJ. 2020. *Ap. J. Lett.* 904:L4
Robin AC, Bienaymé O, Fernández-Trincado JG, Reylé C. 2017. *Astron. Astrophys.* 605:A1
Roth NX, Gibb EL, Bonev BP, et al. 2018. *Astron. J.* 156(6):251
Russell HN. 1916. *Ap. J.* 43:173–96
Sánchez JP, Morante D, Hermosin P, et al. 2021. *Acta Astronaut.* 188:265–77
Schönrich R, Binney J, Asplund M. 2012. *MNRAS* 420(2):1281–93
Sekanina Z. 2019a. arXiv:1903.06300
Sekanina Z. 2019b. arXiv:1905.00935
Seligman D, Laughlin G. 2018. *Astron. J.* 155(5):217
Seligman D, Laughlin G. 2020. *Ap. J. Lett.* 896:L8
Seligman D, Laughlin G, Batygin K. 2019. *Ap. J. Lett.* 876:L26
Seligman DZ, Levine WG, Cabot SHC, Laughlin G, Meech K. 2021. *Ap. J.* 920:28
Seligman DZ, Rogers LA, Cabot SHC, et al. 2022. *Planet. Sci. J.* 3(7):150
Siraj A, Loeb A. 2022. *Ap. J.* 939:53
Skorov Y, Blum J. 2012. *Icarus* 221:1–11
Steckloff JK, Lisse CM, Safrit TK, et al. 2021. *Icarus* 356:113998
Stern SA. 1990. *Icarus* 84(2):447–66
Suyama T, Wada K, Tanaka H. 2008. *Ap. J.* 684(2):1310–22
Tamayo D, Burns JA, Hamilton DP, Hedman MM. 2011. *Icarus* 215:260–78
Taylor AD, Baggaley WJ, Steel DI. 1996. *Nature* 380(6572):323–25
Taylor AG, Seligman DZ, MacAyeal DR, Hainaut OR, Meech KJ. 2023. *Planet. Sci. J.* 4(5):79
Tingay SJ, Kaplan DL, Lenc E, et al. 2018. *Ap. J.* 857:11
Trilling DE, Mommert M, Hora JL, et al. 2018. *Astron. J.* 156:261
Trilling DE, Robinson T, Roegge A, et al. 2017. *Ap. J. Lett.* 850(2):L38

Vaubaillon J. 2022. *WGN J. Int. Meteor Organ.* 50(5):140–43
Villenave M, Ménard F, Dent WRF, et al. 2020. *Astron. Astrophys.* 642:A164
Villenave M, Stapelfeldt KR, Duchêne G, et al. 2022. *Ap. J.* 930:11
Vokrouhlický D, Bottke WF, Chesley SR, Scheeres DJ, Statler TS. 2015. In *Asteroids IV*, ed. P Michel, FE DeMeo, WF Bottke, pp. 509–31. Tucson, AZ: Univ. Ariz. Press
Volk K, Malhotra R. 2008. *Ap. J.* 687:714–25
Warner BD, Harris AW, Pravec P. 2009. *Icarus* 202:134–46
Weaver HA, A'Hearn MF, Arpigny C, et al. 1995. *Science* 267(5202):1282–88
Weryk RJ, Brown P. 2004. *Earth Moon Planets* 95(1–4):221–27
Wiegert PA. 2014. *Icarus* 242:112–21
Williams GV, Sato H, Sarneczky K, et al. 2017. *Cent. Bur. Electron. Telegr.* 4450:1
Wilson TG, Rawlings JMC, Swinyard BM. 2017. *MNRAS* 466(2):1954–62
Xing Z, Bodewits D, Noonan J, Bannister MT. 2020. *Ap. J. Lett.* 893(2):L48
Yang B, Li A, Cordiner MA, et al. 2021. *Nat. Astron.* 5:847
Ye QZ, Zhang Q, Kelley MSP, Brown PG. 2017. *Ap. J. Lett.* 851:L5
Youdin AN, Goodman J. 2005. *Ap. J.* 620:459–69
Zhang Q. 2018. *Ap. J. Lett.* 852:L13
Zhang Y, Lin DNC. 2020. *Nat. Astron.* 4:852–60
Zhou WH, Liu SF, Zhang Y, Lin DNC. 2022. *Astron. Astrophys.* 667:A108